CrossMark

# Estimating the Ultraviolet Emission of M Dwarfs with Exoplanets from Ca II and Hα

Katherine Melbourne[1,2] , Allison Youngblood[3,4] , Kevin France[4] , C. S. Froning[5] , J. Sebastian Pineda[4] ,
Evgenya L. Shkolnik[6] , David J. Wilson[5] , Brian E. Wood[7] , Sarbani Basu[1] , Aki Roberge[8] , Joshua E. Schlieder[8] ,
P. Wilson Cauley[4] , R. O. Parke Loyd[6] , Elisabeth R. Newton[9] , Adam Schneider[6] , Nicole Arulanantham[4] ,
Zachory Berta-Thompson[10] , Alexander Brown[11] , Andrea P. Buccino[12] , Eliza Kempton[13] , Jeffrey L. Linsky[14] ,
Sarah E. Logsdon[8,15] , Pablo Mauas[12] , Isabella Pagano[16] , Sarah Peacock[17] , Seth Redfield[18] , Sarah Rugheimer[19] ,
P. Christian Schneider[20] , D. J. Teal[3,13] , Feng Tian[21] , Dennis Tilipman[10] , and Mariela Vieytes[12,22]
[1] Astronomy Department, Yale University, 52 Hillhouse Avenue, New Haven, CT 06511, USA; melbournekatherine@gmail.com
[2] Ball Aerospace & Technologies Corp., 1600 Commerce Street, Boulder, CO 80301, USA
[3] NASA Goddard Space Flight Center, Greenbelt, MD 20771, USA
[4] Laboratory for Atmospheric and Space Physics, University of Colorado, 600 UCB, Boulder, CO 80309, USA
[5] McDonald Observatory, University of Texas at Austin, Austin, TX 78712, USA
[6] School of Earth and Space Exploration, Arizona State University, 781 Terrace Mall, Tempe, AZ 85287, USA
[7] Naval Research Laboratory, Space Science Division, Washington, DC 20375, USA
[8] Exoplanets and Stellar Astrophysics Lab, NASA Goddard Space Flight Center, Greenbelt, MD 20771, USA
[9] Department of Physics and Astronomy, Dartmouth College, Hanover, NH 03755, USA
[10] Department of Astrophysical & Planetary Sciences, University of Colorado, 391 UCB 2000, Boulder, CO 80309, USA
[11] Center for Astrophysics and Space Astronomy, University of Colorado, 389 UCB, Boulder, Colorado 80309, USA
[12] Instituto de Astronomia y Fisica del Espacio (CONICET–UBA), Buenos Aires, Argentina
[13] University of Maryland, College Park, MD 20742, USA
[14] Joint Institute for Laboratory Astrophysics, University of Colorado and NIST, Boulder, CO 80309-0440, USA
[15] NSF's National Optical-Infrared Astronomy Research Laboratory, 950 N. Cherry Avenue, Tucson, AZ 85719, USA
[16] Istituto Nazionale di Astrofisica, Osservatorio Astrofisico di Catania, Via S. Sofia 78, I-95123, Catania, Italy
[17] Lunar and Planetary Laboratory, University of Arizona, 1629 E. University Boulevard, Tucson, AZ 8572, USA
[18] Astronomy Department and Van Vleck Observatory, Wesleyan University, Middletown, CT 06459, USA
[19] University of Oxford, Atmospheric, Oceanic, and Planetary Physics Department, Clarendon Laboratory, Sherrington Road, Oxford OX1 3PU, UK
[20] Hamburger Sternwarte, Gojenbergsweg 112, D-21029 Hamburg, Germany
[21] Macau University of Science and Technology, Avenida Wai Long, Taipa, Macau
[22] Universidad Nacional de Tres de Febrero, 2736, AHF, Av. Gral. Mosconi, B1674 Sáenz Peña, Buenos Aires, Argentina

## Abstract

M dwarf stars are excellent candidates around which to search for exoplanets, including temperate, Earth-sized planets. To evaluate the photochemistry of the planetary atmosphere, it is essential to characterize the UV spectral energy distribution of the planet's host star. This wavelength regime is important because molecules in the planetary atmosphere such as oxygen and ozone have highly wavelength-dependent absorption cross sections that peak in the UV (900–3200 Å). We seek to provide a broadly applicable method of estimating the UV emission of an M dwarf, without direct UV data, by identifying a relationship between noncontemporaneous optical and UV observations. Our work uses the largest sample of M dwarf star far- and near-UV observations yet assembled. We evaluate three commonly observed optical chromospheric activity indices—Hα equivalent widths and $\log_{10} L_{H\alpha}/L_{bol}$, and the Mount Wilson Ca II H&K $S$ and $R'_{HK}$ indices—using optical spectra from the HARPS, UVES, and HIRES archives and new HIRES spectra. Archival and new Hubble Space Telescope COS and STIS spectra are used to measure line fluxes for the brightest chromospheric and transition region emission lines between 1200 and 2800 Å. Our results show a correlation between UV emission-line luminosity normalized to the stellar bolometric luminosity and Ca II $R'_{HK}$ with standard deviations of 0.31–0.61 dex (factors of ∼2–4) about the best-fit lines. We also find correlations between normalized UV line luminosity and Hα $\log_{10} L_{H\alpha}/L_{bol}$ and the $S$ index. These relationships allow one to estimate the average UV emission from M0 to M9 dwarfs when UV data are not available.

*Unified Astronomy Thesaurus concepts:* Exoplanet atmospheres (487); M dwarf stars (982); Stellar chromospheres (230); Hubble Space Telescope (761); Ultraviolet observatories (1739); Optical observatories (1170); Stellar activity (1580)

*Supporting material:* interactive figures, machine-readable table

## 1. Introduction

M dwarfs ($M_\star \lesssim 0.6 M_\odot$) are excellent candidates for ongoing exoplanet detection and characterization efforts (Shields et al. 2016; Tarter et al. 2007). These are the most abundant stars in the stellar neighborhood (RECONS Survey[23]), making up ∼75% of the Galaxy's total stellar population (Reid & Gizis 1997;

Bochanski et al. 2010). M dwarfs are known to harbor larger populations of small and terrestrial planets relative to solar-type stars (Batalha et al. 2013; Dressing & Charbonneau 2015). The signals from planets orbiting M dwarfs are larger and easier to identify for both the transit and radial velocity methods, the two most commonly used techniques for finding exoplanets. In addition, the long lifetime of an M dwarf (on the order of $10^{12}$ years (Laughlin et al. 1997) for the lowest mass stars) provides ample time for planets to form and life to evolve. Despite

---

[23] www.recons.org

concerns about extreme ultraviolet (EUV) emission, frequent energetic flares, coronal mass ejections, and possible tidal locking, which could alter the atmosphere of an exoplanet orbiting an M dwarf (see Shields et al. 2016 and references within), these smaller, dimmer stars remain a priority in current exoplanet detection efforts due to their many advantages.

The high-energy radiative environment around M dwarfs can significantly impact the upper atmospheric temperature and chemistry of the exoplanets orbiting them (Segura et al. 2005; Lammer et al. 2007; Miguel et al. 2015; Rugheimer et al. 2015; Arney et al. 2017). Quantifying the $\sim$1200–1700 Å (far-UV, FUV, hereafter) and 1700–3200 Å (near-UV, NUV) wavelength ranges of the ultraviolet emission of an M dwarf is essential to assessing any photochemical byproducts (e.g., hazes, biosignatures) in the atmospheres of its exoplanets (Shields et al. 2016; Meadows et al. 2018). In addition, knowledge of an M dwarf's FUV and NUV radiation environment allows for the estimation of EUV emission (Sanz-Forcada et al. 2011; Chadney et al. 2015; Linsky et al. 2013; France et al. 2018; Peacock et al. 2019). This is significant because EUV observations cannot be taken directly for stars other than the Sun; there is no current dedicated mission yet that observes 170–900 Å, and interstellar medium (ISM) attenuation makes observations between $\sim$500–911 Å infeasible for many stars.

M dwarfs have bolometric luminosities ranging from $\sim 10^{-4}$–$10^{-1} L_{\odot}$, moving the location of cool exoplanets (including liquid-water habitable zone (HZ) planets) 5 to 100 times closer around an M dwarf than the comparable orbital separation from the Sun. Combining this with the relatively high UV fluxes of M dwarfs, the incident FUV fluxes are generally higher for cool planets ($T_{\mathrm{equil}} \lesssim 1000$ K) orbiting M dwarfs than they would be around stars of other spectral classes. Photochemical processes depend on the FUV to NUV flux ratio (France et al. 2013; Loyd et al. 2016) and can influence the formation of hazes (Morley et al. 2013, 2015; Crossfield & Kreidberg 2017; Libby-Roberts et al. 2020) as well as the abundances of key biosignatures ($O_2$, $O_3$, and $CH_4$) and habitability indicators ($CO_2$ and $H_2O$) in exoplanet atmospheres around M dwarfs (Hu et al. 2012; Tian et al. 2013; Domagal-Goldman et al. 2014; Wordsworth & Pierrehumbert 2014; Gao et al. 2015; Harman et al. 2015; Luger & Barnes 2015). For example, Ly$\alpha$ (Ly$\alpha$ = 1215.67), the brightest UV emission line in an M dwarf spectrum, has been shown to significantly alter the $H_2O$ mixing ratios within the atmosphere of a mini Neptune orbiting its M dwarf host (Miguel et al. 2015). As $H_2O$ and $CO_2$ in a terrestrial planet atmosphere absorb Ly$\alpha$ radiation from the M dwarf, they dissociate, creating free H and O atoms and OH and CO molecules, leading to catalytic cycles that can produce false-positive and false-negative biosignatures (Harman et al. 2015; Miguel et al. 2015; Rugheimer et al. 2015). UV radiation also leads to the formation of organic hazes in rocky planet atmospheres (Arney et al. 2017) as well as hazes in gaseous planets. Haze strongly affects an exoplanet's spectral features as well as habitability (Arney et al. 2018; Hörst et al. 2018), and an accurate UV spectrum is critical to haze formation modeling.

To analyze exoplanet atmospheres and identify potential false-positive biosignatures, it is essential to characterize the spectral energy distributions (SEDs) of M dwarf hosts, as the cross sections of important molecules and atoms are highly wavelength dependent and peak in the UV (Hu et al. 2012). Most stellar models do not extend beyond the photosphere (Husser et al. 2013; Allard et al. 2012; Hauschildt et al. 1999), thus excluding the primary regions of UV emission. Some progress has been made in including chromospheres, transition regions, and coronae for models of individual stars (Fontenla et al. 2016; Peacock et al. 2019), but those methods are not yet broadly applicable. As a result, SEDs must be directly observed to measure the FUV and NUV activity of a specific star. This requires dedicated space-based UV telescopes and underscores the importance of current observations by the Hubble Space Telescope (HST; France et al. 2016; Guinan et al. 2016; Loyd et al. 2018a; Ribas et al. 2017). However, there may be a gap in observing capability for UV characterization after HST stops UV observations in the coming years. As the Transiting Exoplanet Survey Satellite has completed its primary mission, the Characterizing Exoplanets Satellite has completed its commissioning, the James Webb Space Telescope (JWST) launch approaches, and the extremely large telescopes prepare to begin operations in the late 2020s, a lapse in UV spectral data would limit the characterization of exoplanets discovered with these instruments. Consequently, it is crucial to identify an alternative approach to estimating the UV emission of M dwarfs from optical data measured with ground-based observatories.

Past research has demonstrated the effectiveness of using the Ca II H&K resonance lines (3969 Å, 3934 Å) as indicators for stellar activity (e.g., Wilson 1963; Cincunegui et al. 2007a; Walkowicz & Hawley 2009). Ca II H&K lines appear against the continuum as a superposition of broad $Ca^+$ absorption ($>1$ Å) from the cool upper photosphere and lower chromosphere as well as narrow $Ca^+$ emission ($<-0.5$ Å) from the hot upper chromosphere (Fontenla et al. 2016). Ca II H&K emission has been studied in detail since the Mount Wilson observing program in the 1960s (Wilson 1968) through two stellar activity indices: the $S$ index that includes both chromospheric and photospheric emissions, and $R'_{\mathrm{HK}}$, a transformation of the $S$ index that is normalized to the bolometric flux. This enables comparisons between different spectral types by excluding the contribution of photospheric emission to the measured $S$ index. The $S$ index is only a normalized measure of the line core emission and does not provide a value for the absolute energy emitted in the line, so it is essential to determine $R'_{\mathrm{HK}}$ as well. The program at Mount Wilson defined the $S$ index and $R'_{\mathrm{HK}}$ exclusively using observations of F, G, and K stars, and until recently, the color indices used to calculate these parameters had not been well calibrated for M dwarfs. Cincunegui et al. (2007b) and Suárez Mascareño et al. (2015) used flux-calibrated observations to extend to M dwarfs the color correction factors needed to correct the $S$ index for spectral type effects. Astudillo-Defru et al. (2016) reexamined both the $S$ index and $R'_{\mathrm{HK}}$ Ca II H&K activity tracers for FGK stars and identified an improved method of accurately calculating the $S$ index and $R'_{\mathrm{HK}}$ for M dwarfs, which we follow in this paper.

The H$\alpha$ (6562.8 Å) equivalent width (EW) and H$\alpha$ luminosity normalized to the stellar bolometric luminosity ($\log_{10}(L_{\mathrm{H}\alpha}/L_{\mathrm{bol}})$) were selected for this work as they are also a commonly used indicator for stellar activity, and measurements are widely available in the literature (Reid et al. 1995;

Gizis et al. 2002; West et al. 2011; Douglas et al. 2014; Gaidos et al. 2014; Alonso-Floriano et al. 2015; Newton et al. 2017). Hα traces the top of the chromosphere (Mauas & Falchi 1994, 1996; Leenaarts et al. 2012). All M dwarfs appear to emit significant UV radiation (France et al. 2016), but they are still categorized in the literature as being either "active" or "inactive" depending on each star's Hα emission. For stars in the "inactive" regime (Hα EW > −1 Å, i.e., in absorption), including a significant fraction of the stellar sample used for this work, Hα has been shown to be nonmonotonic with stellar activity (Cram & Mullan 1985; Stauffer & Hartmann 1986) and therefore may not be a precise tracer of UV activity. However, Newton et al. (2017) showed $\log_{10}(L_{\mathrm{H}\alpha}/L_{\mathrm{bol}})$ to be significantly correlated with the stellar rotation period.

The correlation between M dwarf chromospheric optical and UV emission has been demonstrated previously (e.g., Hα-C IV, Hα-Mg II, Ca II K-Mg II, and Ca II K with several Balmer lines; Hawley & Pettersen 1991; Hawley & Johns-Krull 2003; Walkowicz & Hawley 2008; Youngblood et al. 2017). Youngblood et al. (2017) identified the relationships between Ca II and nine UV spectral lines for 15 M dwarfs from 1200 to 2800 Å. In this paper, we expand the sample to 69 M dwarfs and increase the range of activity levels, spectral types, and ages of the stellar sample.

This paper is organized as follows: Section 2 details the M dwarf target selection and the observations used for the analysis in this work. Sections 2.3 and 2.4 discuss how measurements of each optical activity index were found with spectral analysis of the Hα and Ca II H&K lines, respectively. Section 2 also includes a description of how the UV emission-line fluxes were determined. Section 3 describes the correlations found between each optical activity indicator and each UV emission line. We conclude with a discussion of these results in Section 4 and a summary of the findings in Section 5.

## 2. Observations and Reductions

The M dwarfs analyzed in this work were chosen based on the availability of UV spectra from HST and Ca II and/or Hα spectra from high-resolution optical spectrographs like HARPS, HIRES, and UVES. Many of the UV spectra came from recent HST guest observer programs, including the MUSCLES Treasury Survey (GO 13650; France et al. 2016; Loyd et al. 2016; Youngblood et al. 2016), the Mega-MUSCLES Treasury Survey (GO 15071; Froning et al. 2019), the Far Ultraviolet M-dwarf Evolution Survey (FUMES; GO 14640; J. S. Pineda et al. 2020, in preparation), the Habitable Zones and M dwarf Activity across Time (HAZ-MAT) survey (GO 14784; Loyd et al. 2018a), and the M Dwarf Stellar Wind survey (GO 15326; B. E. Wood et al. 2020, in preparation). Our targets range in spectral type from M0 to M9, and all but one target observed are within $d < 60$ pc of Earth. The sample covers a wide range of ages (~0.01 to ~10 Gyr): several stars in the TW Hya association are likely the youngest stars (~10 Myr; Weinberger et al. 2012) and Barnard's Star and Kapteyn's Star are likely the oldest stars (~10 Gyr; Kotoneva et al. 2005; Wylie-De Boer et al. 2010; Ribas et al. 2018). Figure 1 provides a visual of the range of radii, effective temperatures, and $R'_{\mathrm{HK}}$; other details about each target may be found in Tables 1 and 2. Ages were gathered from the literature, where they were established through membership to young moving groups or clusters or galactic kinematics. In the

absence of any age information, targets are assumed to be field age (~5 Gyr).

### 2.1. Optical Data

For the optical spectra, we used public archival data from three ground-based observatories, the High Accuracy Radial velocity Planet Searcher (HARPS) on the ESO 3.6 m telescope (Mayor et al. 2003), the Ultraviolet and Echelle Spectrograph (UVES) on the Very Large Telescope (Dekker et al. 2000), and the High Resolution Echelle Spectrometer (HIRES) on the Keck I Telescope (Vogt et al. 1994). HARPS (S1D) and UVES one-dimensional merged spectra were downloaded from the ESO archive. We also obtained new Keck/HIRES spectra of M dwarfs with available UV spectra but no Ca II H&K spectra. We were awarded three half-nights (2019 March 1, 2019 July 7, and 2019 July 8). We used the HIRES blue arm with the C5 decker (1″148 × 7″ slit), the KV370 filter, echelle angle = 0°046918, cross-dispersion angle = 1°9523, and standard 2 × 1 binning. The nominal spectral resolving power of this mode is $R = 37,000$. We obtained new spectra covering wavelengths 3750–6720 Å for four M dwarfs (LP 5-282, G75-55, LP 247-13, GJ 3290), and we use the data products from the automatic pipeline MAKEE[24] as were used for all archival HIRES spectra used in this work. For targets with no available optical spectra with sufficient signal-to-noise (S/N) from HARPS, HIRES, or UVES, we used single spectra available to our team from the Canada–France–Hawaii Telescope ESPaDOnS spectrograph[25] (2MASS J02001277–0840516 and GJ 3997) and the Observatoire de Haute-Provence ELODIE spectrograph[26] (2MASS J04223953+1816097 and 2MASS J04184702+1321585; Moultaka et al. 2004).

We did not flux-calibrate any of our optical spectra; the activity indicators used rely on normalizations to nearby continua, and we compared our measurements to overlapping samples from Newton et al. (2017) and Astudillo-Defru et al. (2016) to ensure our technique is in line with theirs. To account for the time variability of stellar activity levels with noncontemporaneous observations, we found the optical activity indices of each spectrum individually and took the S/N weighted average for the final result (described in Sections 2.3 and 2.4). Errors calculated for the optical parameters of our target sample do not take into account stellar variability, and not all stars were observed over multiple epochs. Measurements for a representative sample from our target list are shown in Figure 2.

### 2.2. Ultraviolet Data

Ultraviolet spectra came from the Hubble Space Telescope (HST) Space Telescope Imaging Spectrograph (STIS) and Cosmic Origins Spectrograph (COS). A variety of gratings and central wavelength settings (noted as the grating with central wavelength setting in parentheses) were used in this diverse data set, including G140L (1425 Å), G140M (1222 Å), E140M (1425 Å), E140H (1271 Å), G230L (2950 Å), E230M (2707 Å), and E230H (2713 Å) for STIS, and G140L (1105, 1230, and 1280 Å), G130M (1222, 1291, 1309, 1318, and 1327 Å), G160M (1533, 1577, 1589, 1600, 1611, and 1623 Å),

---

[24] http://www.astro.caltech.edu/~tb/makee/
[25] http://www.cadc-ccda.hia-iha.nrc-cnrc.gc.ca/en/cfht/
[26] http://atlas.obs-hp.fr/elodie/

Table 1
The M Dwarf Sample

| Star | Star | Star | Star |
|------|------|------|------|
| GO 13650 (MUSCLES)[1] | GJ 173 | AR 10638 (STARCat)[5] | GO 9090[11] |
| GJ 176 | GJ 3290 | GJ 388 | GJ 285 |
| GJ 667C | LP 5-282 | GJ 803 | GJ 644C |
| GJ 581 | 2MASS J04223953+1816097 | GJ 873 | |
| GJ 1214 | 2MASS J04184702+1321585 | GJ 551 | GO 15071 (Mega- |
| GJ 832 | 2MASS J02125819−5851182 | | MUSCLES)[12] |
| GJ 876 | GJ 3997 | GO 14462[6] | TRAPPIST-1 |
| GJ 436 | 2MASS J22463471−7353504 | GJ 1132 | GJ 676 A |
| GJ 628 | | | GJ 15A |
| GJ 887 | GO 14640 (FUMES)[3] | GO 14767 (PanCET)[7] | GJ 649 |
| GJ 1061 | GJ 4334 | GJ 3470 | GJ 163 |
| HD 173739 | GJ 49 | | GJ 849 |
| | GSC 07501-00987 | GO 12361[8] | GJ 674 |
| GO 14784 (HAZMAT)[2] | LP 247-13 | TWA 13A | GJ 699 |
| GSC 8056-0482 | G80-21 | TWA 13B | LHS 2686 |
| 2MASS J02543316−5108313 | CD-571054 | | GJ729 |
| 2MASS J02001277−0840516 | CD-352722 | GO 11616[9] | |
| G75-55 | GJ 410 | TWA 7 | GO 15326[13] |
| 2MASS J22025453−6440441 | LP 55-41 | | GJ 273 |
| 2MASS J00240899−6211042 | G249-11 | GO 12011[10] | GJ 205 |
| 2MASS J01521830−5950168 | | LHS 2065 | GJ 588 |
| 2MASS J03315564−4359135 | GO 13020 (Living with | LHS 3003 | GJ 338A |
| 2MASS J23261069−7323498 | a Red Dwarf)[4] | | |
| 2MASS J23285763−6802338 | GJ 191 | | GO 15190[14] |
| 2MASS J00393579−3816584 | | | GJ 411 |

**Note.** (1) France et al. (2016), (2) Loyd et al. (2018a), (3) J. S. Pineda et al. (2020, in preparation), (4) Guinan et al. (2016), (5) Ayres (2010), (6) Waalkes et al. (2019), (7) Sing et al. (2019), (8) PI: Brown, (9) France et al. (2012), (10) PI: Osten, (11) Hawley & Johns-Krull (2003), (12) Froning et al. (2019), (13) B. E. Wood et al. (2020, in preparation), (14) A. Youngblood et al. (2020, in preparation).
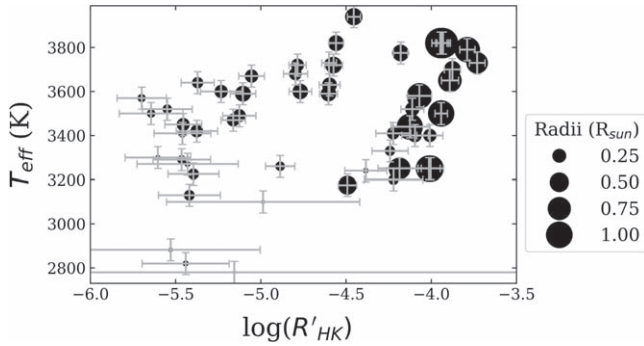


**Figure 1.** The M dwarf sample studied in this work spans a range of ∼1000 K in effective temperature, with an assumed uncertainty of ±50 K on each value, and ∼3 dex in activity levels as represented by the log $R'_{HK}$ values (see Section 2.4). The relative radius of each star is demonstrated by the size of the points, with a range of 0.11 to 1.07 $R_\odot$. Young, early M dwarfs that have radii around 1 $R_\odot$ are included in this sample (see Table 2 for further clarification). This plot shows the 45 stars (of 69 total targets) for which an $R'_{HK}$ value is reported in this work.

and G230L (2376, 2635, 2950, and 3360 Å) for COS. We used spectra downloaded from MAST reduced with the standard STScI pipeline, except for spectra from the MUSCLES and Mega-MUSCLES Treasury Surveys (Wilson et al. 2020, in review; France et al. 2016; Loyd et al. 2016; Youngblood et al. 2016; Froning et al. 2019), FUMES (J. S. Pineda et al., 2020 in preparation), and the STARCat catalog (Ayres 2010); see references for descriptions of the data reduction. Similarly, data from GO 15190 and GO 15326 were reduced using the same methods used in the STARCat catalog.

For the UV spectra, we took the error-weighted average of all available spectra before measuring each spectral line, because the S/N of each UV spectrum was generally lower. To measure the flux of the UV emission lines not found in previous literature (noted in Table 3), we fit a Voigt profile, because it accurately captures the core and the wings of each line and requires only four parameters, allowing for computational efficiency. For the pair of blended lines that comprise Si II and Mg II, we fit a double Gaussian because the wings of these lines are typically below the instrumental noise floor. Uncertainty for each Voigt parameter and the integrated line flux were determined by bootstrapping: we randomly sampled with replacement the flux values for each line and fit a Voigt profile to each new sample. Although we considered block bootstrapping—resampling data pairs with replacement in subsections of each spectral line range that have similar noise profiles—we determined there was no effect on our results and therefore resampled across the entire wavelength range for each spectral line. We report the median and standard deviation of the set of Voigt integral flux and the error. In Section 3, we use the UV line luminosities normalized to the stellar bolometric luminosity, which we calculate as $L_{bol} = \sigma_{SB}T_{eff}^4 \, 4\pi R_\star^2$ using stellar parameters from Table 2. Uncertainties in our $T_{eff}$ and $R_\star$ parameters range from 1%–5% and 1%–10%, respectively. In particular, the largest stars in our sample (2MASS J01521830 −5950168, 2MASS J03315564−4359135, and 2MASS J23261069−7323498) have 1.07 ± −0.17 $R_\odot$ (Malo et al. 2014b).

Absorption from gaseous species in the interstellar medium has at least some effect on the majority of the UV emission lines analyzed, including Lyα, Mg II, C II, Si II, and Si III. For

**Table 2**
M Dwarf Parameters, Optical Activity Indicators, and UV Luminosities

| Column | Format | Units | Description |
| --- | --- | --- | --- |
| 1 | str | ⋯ | Target name |
| 2 | int | ⋯ | Identifier used in the paper |
| 3 | flt | pc | Stellar distance |
| 4 | str | ⋯ | ADS bibliography code reference for distance |
| 5 | str | ⋯ | Stellar spectral type |
| 6 | str | ⋯ | ADS bibliography code reference for spectral type |
| 7 | flt | K | Stellar effective temperature |
| 8 | str | ⋯ | ADS bibliography code reference for effective temperature |
| 9 | flt | $R_\odot$ | Stellar radius |
| 10 | str | ⋯ | ADS bibliography code reference for radius |
| 11 | flt | mag | $V$ magnitude |
| 12 | str | ⋯ | ADS bibliography code reference for $V$ |
| 13 | flt | mag | $K$ magnitude |
| 14 | str | ⋯ | ADS bibliography code reference for $K$ |
| 15 | flt | Gyr | Stellar age |
| 16 | str | ⋯ | ADS bibliography code reference for age |
| 17 | flt | 0.1 nm | H$\alpha$ equivalent width |
| 18 | flt | 0.1 nm | Uncertainty in H$\alpha$ equivalent width |
| 19 | str | ⋯ | ADS bibliography code reference for H$\alpha$ |
| 20 | flt | ⋯ | $S$ index |
| 21 | flt | ⋯ | Uncertainty in $S$ index |
| 22 | flt | ⋯ | $\log_{10} R'_{\rm HK}$ |
| 23 | flt | ⋯ | Uncertainty in $\log_{10} R'_{\rm HK}$ |
| 24 | str | ⋯ | ADS bibliography code reference for the $S$ index and $\log_{10} R'_{\rm HK}$ |
| 25 | str | ⋯ | Instruments used for optical activity indicators (H = HARPS, K = HIRES, U = UVES, M = MIKE, E = ELODIE, S = ESPaDOnS) |
| 26 | flt | ⋯ | Number of H$\alpha$ spectra used |
| 27 | flt | ⋯ | Number of Ca II spectra used |
| 28 | flt | erg s$^{-1}$ | Si III Luminosity |
| 29 | flt | erg s$^{-1}$ | Si III Luminosity uncertainty |
| 30 | str | ⋯ | ADS bibliography code reference for Si III |
| 31 | flt | erg s$^{-1}$ | Ly$\alpha$ luminosity |
| 32 | flt | erg s$^{-1}$ | Ly$\alpha$ luminosity uncertainty |
| 33 | str | ⋯ | ADS bibliography code reference for Ly$\alpha$ |
| 34 | flt | erg s$^{-1}$ | Si II luminosity |
| 35 | flt | erg s$^{-1}$ | Si II luminosity uncertainty |
| 36 | str | ⋯ | ADS bibliography code reference for Si II |
| 37 | flt | erg s$^{-1}$ | C II (1335 Å) luminosity |
| 38 | flt | erg s$^{-1}$ | C II (1335 Å) Luminosity uncertainty |
| 39 | str | ⋯ | ADS bibliography code reference for C II |
| 40 | flt | erg s$^{-1}$ | Mg II luminosity |
| 41 | flt | erg s$^{-1}$ | Mg II luminosity uncertainty |
| 42 | str | ⋯ | ADS bibliography code reference for Mg II |
| 43 | flt | erg s$^{-1}$ | Si IV luminosity |
| 44 | flt | erg s$^{-1}$ | Si IV luminosity uncertainty |
| 45 | str | ⋯ | ADS bibliography code reference for Si IV |
| 46 | flt | erg s$^{-1}$ | He II luminosity |
| 47 | flt | erg s$^{-1}$ | He II luminosity uncertainty |
| 48 | str | ⋯ | ADS bibliography code reference for He II |
| 49 | flt | erg s$^{-1}$ | C IV luminosity |
| 50 | flt | erg s$^{-1}$ | C IV luminosity uncertainty |
| 51 | str | ⋯ | ADS bibliography code reference for C IV |

| Column | Format | Units | Description |
| --- | --- | --- | --- |
| 52 | flt | erg s$^{-1}$ | N V luminosity |
| 53 | flt | erg s$^{-1}$ | N V luminosity uncertainty |
| 54 | str | ⋯ | ADS bibliography code reference for N V |

**References.** Upgren et al. (1972), Joy & Abt (1974), Kukarkin et al. (1981), Walker (1983), Oja (1985), Mermilliod (1986), D'Antona (1986), Kirkpatrick et al. (1991), Martin et al. (1994), Hawley et al. (1996), Gizis (1997), Beuermann et al. (1999), Høg et al. (2000), Henry et al. (2002), Ducati (2002), Ségransan et al. (2003), Cruz et al. (2003), Hawley & Johns-Krull (2003), Cutri et al. (2003), Reid et al. (2004), Kotoneva et al. (2005), Scholz et al. (2005), Bonfils et al. (2005), Costa et al. (2005), Rivera et al. (2005), Wood et al. (2005), Reid & Gizis (2005), Torres et al. (2006), Riaz et al. (2006), Costa et al. (2006), Woolf & Wallerstein (2006), Butler et al. (2006), van Leeuwen (2007), Wargelin et al. (2008), Torres et al. (2008), Demory et al. (2009), Landolt (2009), van Belle & von Braun (2009), Plavchan et al. (2009), Shkolnik et al. (2009), Osten et al. (2010), Sanz-Forcada et al. (2010), Koen et al. (2010), Houdebine (2010), Stauffer et al. (2010), Röser et al. (2011), Lépine & Gaidos (2011), Irwin et al. (2011), Kraus et al. (2011), von Braun et al. (2011), Berta et al. (2011), Anglada-Escudé & Tuomi (2012), McCarthy & White (2012), Kiraga (2012), Rojas-Ayala et al. (2012), von Braun et al. (2012), Shkolnik et al. (2012), Santos et al. (2013), Tuomi & Anglada-Escudé (2013), Zacharias et al. (2013), Malo et al. (2013), Weinberger et al. (2013), Pecaut & Mamajek (2013), Neves et al. (2014), Jao et al. (2014), Kraus et al. (2014), Shkolnik & Barman (2014), Finch et al. (2014), Malo et al. (2014a), Loyd & France (2014), von Braun et al. (2014), Biddle et al. (2014), Gaidos et al. (2014), Anglada-Escude et al. (2014), Alonso-Floriano et al. (2015), White et al. (2015), Davison et al. (2015), Newton et al. (2015), Mann et al. (2015), Terrien et al. (2015), Bell et al. (2015), Berta-Thompson et al. (2015), France et al. (2016), Guinan et al. (2016), Houdebine et al. (2016), Youngblood et al. (2016), Bazot et al. (2016), Awiphan et al. (2016), Maldonado et al. (2017), Astudillo-Defru et al. (2016), Miles & Shkolnik (2017), Shkolnik et al. (2017), Dressing et al. (2017), Newton et al. (2017), Riedel et al. (2017), Youngblood et al. (2017), Kruczek et al. (2017), Burgasser & Mamajek (2017), Gaia Collaboration et al. (2018), Bourrier et al. (2018), Schneider & Shkolnik (2018), Dressing et al. (2018), Van Grootel et al. (2018), Gagné & Faherty (2018), France et al. (2018), Zurlo et al. (2018), Ribas et al. (2018), Houdebine et al. (2019), Froning et al. (2019), Dreizler et al. (2020), Linsky et al. (2020).

(This table is available in its entirety in machine-readable form.)

Si III, the effect is expected to be negligible (Redfield & Linsky 2004), so corrections were not applied. The impact on the Si II emission line at 1260 Å by the ISM ranges from negligible to moderate depending on the line of sight (Redfield & Linsky 2004). No correction was applied, and any uncorrected ISM absorption may cause some scatter in our Si II correlations. ISM effects are most noticeable for the Ly$\alpha$ line with complete absorption in the line center caused by optically thick H I. We only use intrinsic Ly$\alpha$ fluxes that have been reconstructed from their observed profiles (Wood et al. 2005; Youngblood et al. 2016, 2017) with typical uncertainties of 5%–30%. The C II 1334 Å line is similarly affected by ISM absorption, so only the flux from the 1335 Å line of the C II doublet is included in the listed C II flux values. Additionally, both lines in the Mg II doublet experience attenuation, which is accounted for by assuming a uniform 30% ± 10% correction to measured values (propagating errors accordingly) based on
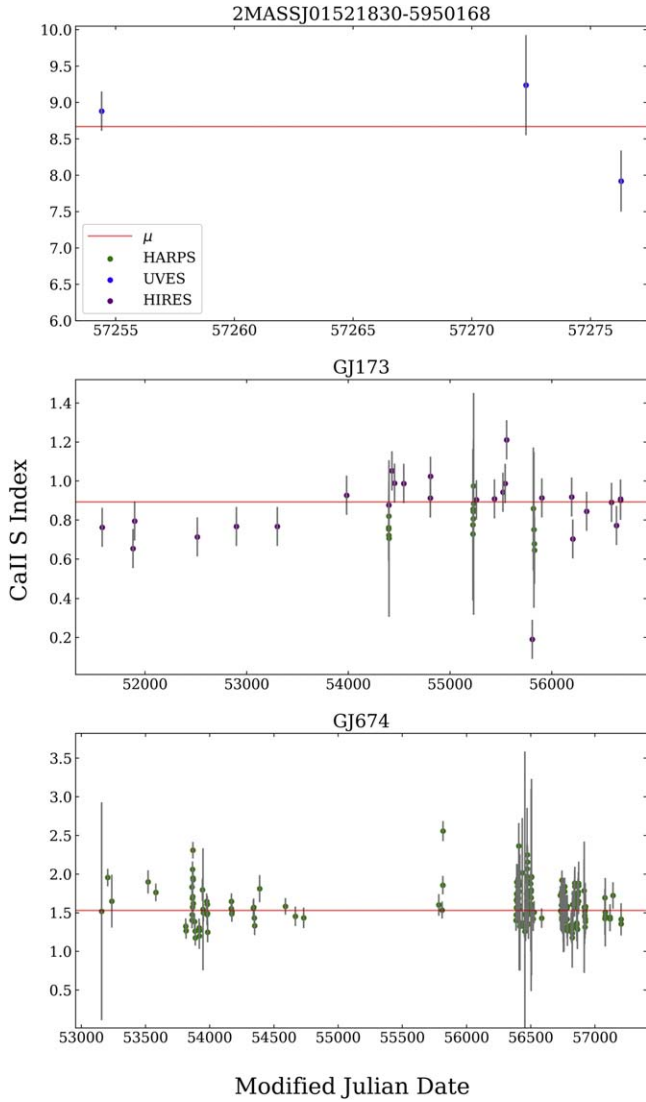
**Figure 2.** Stars representing the range of quantity and quality of *S*-index measurements available for the target stars in our sample. Some, including 2MASS J01521830–5950168 (top panel), have only a few observations in total. Few have been observed by multiple instruments, but GJ 173 is an example of a star observed with both HIRES and HARPS. Finally, GJ 674 shows how some stars have multiple observations in a short amount of time with longer spans without any observations.

assumptions discussed by Redfield & Linsky (2002) and Youngblood et al. (2017). With regard to our optical lines, Ca II can also be absorbed by $Ca^+$ in the ISM, but attenuation is only significant for stars at a distance beyond 100 pc (Fossati et al. 2017), of which there are none in this study.

### 2.3. Hα Equivalent Widths and $log_{10}$ ($L_{Hα}/L_{bol}$)

We measured Hα EWs using the equation

$$EW = \int_{\lambda_1}^{\lambda_2} \left(1 - \frac{F_\lambda}{F_c}\right) d\lambda, \qquad (1)$$

where $F_\lambda$ is the flux of each wavelength across the width of the line and $F_c$ is defined as the average continuum from two ranges on either side of the line, 6500–6550 Å and 6575–6625 Å. For $d\lambda$, we use the average pixel width between each observed wavelength in a spectrum, as variations are negligible. We follow

the method used by West et al. (2011) and Newton et al. (2016) and assign the bounds of integration to be $\lambda_1 = 6558.8$ Å and $\lambda_2 = 6566.8$ Å for all spectra. The EW-weighted means and uncertainties for all targets are listed in Table 2.

We validate our EW measurements by comparing with Newton et al. (2016) Hα EWs (Hα$_N$) for 12 overlapping targets, finding the best-fit line Hα$_N$ = 1.05($\pm$0.003)Hα + 0.04($\pm$0.03). The slight departure from a precise 1:1 line is a result of the use of multiple instruments in our calculations, and no additional calibration was performed to match our measured values to Newton et al. When optical spectra were not available for Hα measurements, we used literature values from Riaz et al. (2006) and Malo et al. (2014a), who used the IRAF splot package to calculate Hα EWs for a sample of M dwarfs. Our calculated values are comparable to those found in the literature (Hα$_{lit}$). Fitting a least-squares linear regression, we found a best-fit line of Hα$_{lit}$ = 0.98($\pm$0.04)Hα – 0.34($\pm$0.41), and therefore, we assume no significant variation in Hα values across both studies and this work.

In order to remove the stellar mass dependence of our Hα index (the Wilson–Bappu effect; Wilson & Vainu Bappu 1957; Stauffer & Hartmann 1986), we calculate $log_{10}$ ($L_{Hα}/L_{bol}$) using the methods of Douglas et al. (2014) and Newton et al. (2017). First, we subtract from our EW measurements the minimum Hα EW value for a star of a given mass using relations from Newton et al. (2017). We estimate the masses of our targets to accuracies of 10%–20% from various literature sources. For the few cases where literature masses were unavailable, we used BT-Settl isochrones[27] (Allard et al. 2012) with solar abundances (Caffau et al. 2010) and the target's effective temperature (Table 2) to determine a mass. We then converted these corrected Hα EWs into $L_{Hα}/L_{Bol}$ by multiplying each EW by a spectral type conversion factor ($\chi$) determined by Douglas et al. (2014).

### 2.4. Ca II H&K Indices

#### 2.4.1. The S Index

The *S* index measures the flux ratio between the Ca II H&K lines and the surrounding continuum, standardized by an instrumental calibration factor (Vaughan et al. 1978). Two triangular bandpasses are centered on the H and K lines with 1.09 Å FWHM, and two 20 Å top-hat bandpasses are centered at 3901 Å and 4001 Å, known as the V and R ranges, respectively (Figure 3). The *S* index is limited in comparing activity levels across spectral types; as the integrated continuum emission decreases for cooler stars, the *S* index will increase (Middlekoop 1982). In addition, the triangular bandpasses include contaminating photospheric emission in addition to the desired chromospheric emission.

We follow the method in Lovis et al. (2011) and Astudillo-Defru et al. (2016) to allow for optimal validation of our measurements, as there is a significant overlap of our data set with theirs. Our measured values are compiled in Table 2. We calculate the *S* index for all of our target stars by determining the mean flux emitted across both 20 Å continuum regions and the 1.09 Å regions centered on each line instead of integrating

---

[27] https://phoenix.ens-lyon.fr/Grids/BT-Settl/CIFIST2011_2015/ISOCHRONES/
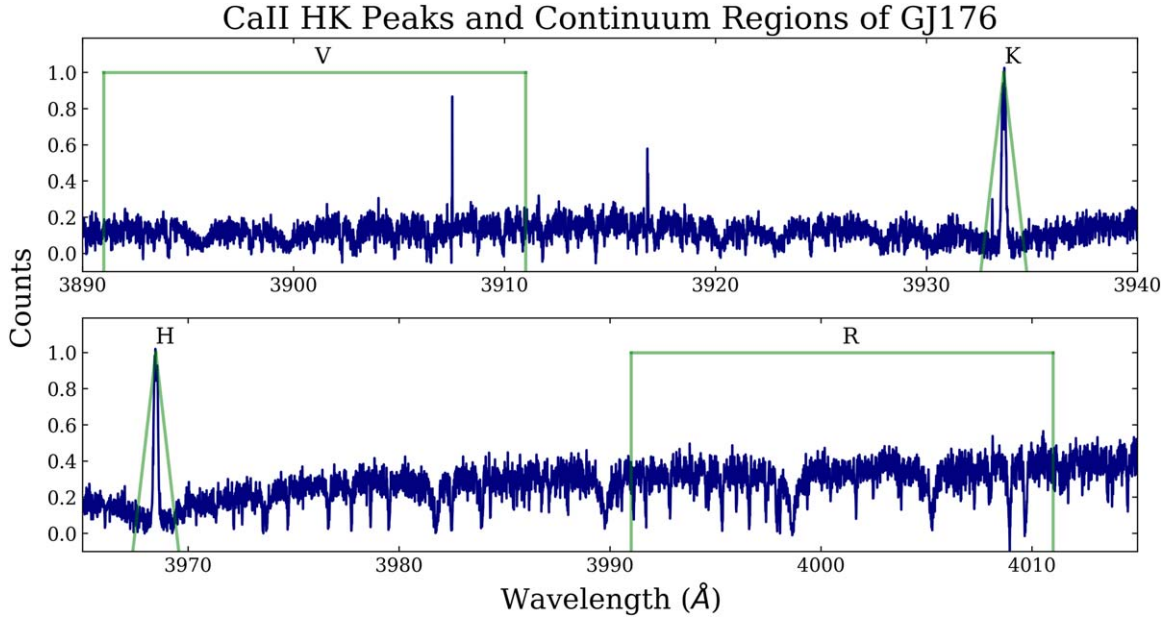
**Figure 3.** Demonstration of continua and triangular passbands used in the Ca II analysis (Wilson 1968; Vaughan et al. 1978). The Ca II H line (3968.47 Å) passband and continuum regions avoid the Hε emission line (3970.07 Å). This figure uses an individual S1D spectrum of GJ 176 observed with HARPS as an example.

**Table 3**
Fit Parameters for $\log_{10} R'_{\mathrm{HK}}$ and $\log_{10} (L_{\mathrm{UV}}/L_{\mathrm{bol}})$

| Transition Name | Wavelength (Å) | $\log T_{\mathrm{formation}}$[a] | $\alpha$ | $\beta$ | $\rho$ | $n$ | $\sigma$ |
|---|---|---|---|---|---|---|---|
| Si III | 1206.50 | 4.7 | $1.47 \pm 0.13$ | $0.42 \pm 0.61$ | 0.80 | $<0.0001$ | 0.50 |
| LyA | 1215.67 | $\lesssim 4.5$ | $1.07 \pm 0.19$ | $0.92 \pm 0.89$ | 0.78 | $<0.0001$ | 0.44 |
| N V | 1238.82, 1242.8060 | 5.2 | $1.53 \pm 0.21$ | $0.8 \pm 0.99$ | 0.76 | $<0.0001$ | 0.58 |
| Si II[b] | 1260.42, 1264.74, 1265.00 | 4.5 | $1.45 \pm 0.26$ | $-0.16 \pm 1.20$ | 0.84 | $<0.0001$ | 0.47 |
| C II[c] | 1335.71 | 4.5 | $1.73 \pm 0.20$ | $1.96 \pm 0.96$ | 0.84 | $<0.0001$ | 0.56 |
| Si IV | 1393.76, 1402.77 | 4.9 | $1.36 \pm 0.11$ | $-0.07 \pm 0.52$ | 0.78 | $<0.0001$ | 0.49 |
| C IV | 1548.19, 1550.78 | 5.0 | $1.43 \pm 0.13$ | $0.86 \pm 0.63$ | 0.78 | $<0.0001$ | 0.48 |
| He II | 1640.4[d] | 4.9 | $1.35 \pm 0.09$ | $0.32 \pm 0.41$ | 0.84 | $<0.0001$ | 0.35 |
| Mg II[b,e] | 2796.35, 2803.53 | $\lesssim 4.5$ | $1.38 \pm 0.17$ | $2.03 \pm 0.80$ | 0.84 | $<0.0001$ | 0.36 |

**Notes.** The scaling relations take the form $\log_{10} L_{\mathrm{UV}} = (\alpha \times \log_{10} R'_{\mathrm{HK}}) + \beta$, where $L_{\mathrm{UV}}$ represents each UV emission-line luminosity in erg s$^{-1}$. $\rho$ is the Spearman correlation coefficient, $n$ is the probability of no correlation, and $\sigma$ is the standard deviation of the data points about the best-fit line (dex).
[a] Formation temperatures are from the CHIANTI database (Dere et al. 1997; Landi et al. 2013). Note that the Ca II H&K line cores form around $10^{3.8}$ K, a similar temperature to the Lyα and Mg II line wings (Vernazza et al. 1981).
[b] Fit with a double Gaussian because wings cannot be resolved at the lower S/N of these blended emission lines.
[c] Due to significant ISM absorption, the 1334.54 Å line was not included.
[d] Average wavelength of the multiplet.
[e] Fluxes uniformly corrected for $30\% \pm 10\%$ ISM absorption (see Section 3 and Youngblood et al. 2016).

over them,

$$S = \alpha \frac{\tilde{f}_H + \tilde{f}_K}{\tilde{f}_V + \tilde{f}_R}, \qquad (2)$$

where $\alpha \approx 1$ and $\tilde{f}_V$, $\tilde{f}_R$, $\tilde{f}_H$, and $\tilde{f}_K$ are the mean flux emitted in the 20 Å continuum regions (V, R) and the 1.09 Å line regions (H, K). To confirm the accuracy of our measurements, we fit a linear least-squares regression of our $S$-index values to the Mount Wilson values provided by Astudillo-Defru et al. (2016; 22 overlapping targets in total) to find the following relation: $S = 1.05(\pm 0.01) S_{\mathrm{orig}} + 0.06(\pm 0.01)$, with $S$ representing the $S$ indices found in their study and $S_{\mathrm{orig}}$ denoting those found in our work. For this comparison, we used $S$-index values found from all three ground-based spectrographs: HARPS, UVES,

and HIRES. There were not enough overlapping observations obtained with these three spectrographs to quantify the differences between the measured $S$ index of individual targets using multiple instruments.

*2.4.2. $R'_{HK}$*

Accurate characterization of the chromospheric activity levels is essential for this work. UV radiation originates in magnetically heated regions of the stellar atmosphere above the photosphere, meaning photospheric emission is not correlated with UV emission lines. Thus, we measure the $R'_{\mathrm{HK}}$ index (Middlekoop 1982; Noyes 1984; Rutten 1984), which includes corrections for the photospheric flux in the continuum (V, R) and line (H, K) regions of the $S$ index. $R'_{\mathrm{HK}}$ has been well-defined for F, G, and K spectral types (Lovis et al. 2011) and has been previously

extrapolated to later spectral types with less accuracy (as discussed in Astudillo-Defru et al. 2016). Past attempts to characterize $R'_{HK}$ for M dwarfs used the original $B - V$ color index (Mittag et al. 2013), which is not best suited for M dwarfs due to their frequent lack of available $B$-band photometry in the literature and $V$ band sensitivity to metallicity (Delfosse et al. 1998; Bonfils et al. 2013; Astudillo-Defru et al. 2016).

$R'_{HK}$ is related to the $S$ index by

$$R'_{HK} = R_{HK} - R_{phot} = K\sigma_{SB}^{-1}10^{-14}C_{cf}(S - S_{phot}), \qquad (3)$$

where $R_{phot}$ and $S_{phot}$ are photospheric contributions to $R'_{HK}$ and $S$, respectively, $\sigma_{SB}$ is the Stefan–Boltzmann constant, $C_{cf}$ is the color correction factor, and $K$ is a factor that transforms arbitrary fluxes to surface fluxes. Middlekoop (1982) and Rutten (1984) both calculated $K$, but $1.07 \times 10^6$ erg cm$^{-2}$ s$^{-1}$ is the most recent value provided in Hall et al. (2007).

In calculating the color correction factor, $C_{cf}$, and $R_{phot}$, we follow Equations (9), (10), and Table 1 from Astudillo-Defru et al. (2016). We elect to use the coefficients provided corresponding to the $V - K$ color index in the Johnson photometric system (Johnson 1966), as $V$-band fluxes are generally more available than $I$ band fluxes. The relations between $V - K$, $C_{cf}$, and $R_{phot}$ are

$$\log C_{cf} = -0.005(V - K)^3 + 0.071(V - K)^2 \\ - 0.713(V - K) + 0.973 \qquad (4)$$

$$\log R_{phot} = -0.003(V - K)^3 + 0.069(V - K)^2 \\ - 0.717(V - K) - 3.498. \qquad (5)$$

A small number of our stars have no $V$-band magnitudes available in the literature, and we calculate the $V$ magnitude from $V - K$ estimates provided by Pecaut & Mamajek (2013). Uncertainties are assumed to be 5% of the flux value; we assumed the same relative error for stars whose $V$ magnitudes have no published uncertainties.

## 3. UV–Optical Relations

We analyzed the relation between each optical activity indicator and the luminosities of nine different UV lines each normalized by the bolometric luminosity (listed in Table 2). For $\log_{10}(L_{H\alpha}/L_{bol})$, the $S$ index, and $R'_{HK}$, power laws were fitted to the data (including uncertainties) in log space using the same bootstrapping method described in Section 2. We resampled the data with replacement and found a best-fit line each time, then found the median and the 68% confidence interval among all the fits performed, shown in Figures 4–6. Tables 3–5 list the fitted power-law parameters for the median line and 1σ uncertainties as well as the Spearman rank-order correlation coefficients ($\rho$), and the standard deviations about the best-fit line.

Figure 4 shows the relation between $\log_{10}(L_{H\alpha}/L_{bol})$ and $\log(L_{UV}/\log L_{bol})$ for each line, and Table 4 describes the fit parameters. We find statistically significant, positive correlations between $\log_{10}(L_{H\alpha}/L_{bol})$ and $\log(L_{UV}/\log L_{bol})$ for all UV emission lines. There are two regions of stars, active (Hα in emission) and inactive (Hα in absorption). The active stars are clustered in the area of each graph in Figure 6 with $\log_{10}(L_{H\alpha}/L_{bol}) > \sim-4$, and the inactive stars are scattered along the rest of the best-fit lines. When analyzed separately, there was no significant correlation in either region; however, our sample spans a wide range of Hα values, which demonstrate a significant correlation when examined together. Mg II has the weakest

correlation with $\log_{10}(L_{H\alpha}/L_{bol})$ and the most uncertain best-fit line of all the UV emission lines, even when excluding the outlier GJ 676 A (Section 3.1) from the fit, due to a lack of stars in our sample that are active in both Mg II and Hα. This is likely because of the recent HST brightness restrictions for M dwarfs that are strictest in the NUV regime, affecting the community's ability to collect Mg II data for more active stars. We present in the caption of Table 4 an alternate fit that parameterizes the apparent flattening of $L(Mg II)/L_{bol}$ in the inactive regime. We have also removed the outlier LP 247-13 from the $L(Ly\alpha)/L_{bol} - \log_{10}(L_{H\alpha}/L_{bol})$ fit because it drives the best-fit slope to a steep value that does not match the other active stars.

Here we describe the comparison between Hα EW and $\log(L_{UV}/\log L_{bol})$, which is not shown because there is no apparent correlation. The targets are divided into two loci: an active and inactive regime. As the EW becomes more negative (more active), the UV luminosity plateaus at a nearly constant high value. For smaller EWs (EW $\sim 0$; less active), there is a large spread of several orders of magnitude in normalized UV luminosity. Our sample has 52 M dwarfs from M0–M5.5 with Hα EWs concentrated near the threshold between active ($<-1$ Å) and inactive ($>-1$ Å) M dwarfs. Hα absorption lines deepen with increased activity before flipping to emission (Cram & Mullan 1985), leading to a nonmonotonic relation between stellar activity and Hα EW whereas UV emission scales monotonically with stellar activity. This mostly affects stars with Hα EWs $\gtrsim-1$ Å, making Hα EW a poor activity indicator for inactive M dwarfs (Walkowicz & Hawley 2008).

The relationships between the $\log S$ index and $\log(L_{UV}/\log L_{bol})$ line emissions are shown in Figure 5. The $S$ index includes photospheric contamination that leads to a wider spread of UV flux values at each $S$ index, as the UV lines do not originate in the photosphere (e.g., Vernazza et al. 1981). Because of this, we did not expect a tight correlation with UV luminosity, but the Spearman rank-order correlation coefficients indicate a statistically significant positive correlation for each emission line. Parameters for the best-fit lines are shown in Table 5. The scatter about the $S$-index best-fit lines are greater than about the $\log_{10}(L_{H\alpha}/L_{bol})$ best-fit lines for all emission lines except Mg II.

Transforming the $S$ index to $R'_{HK}$ removes the unwanted photospheric contribution that is present in the $S$ index. Because the UV emission lines studied originate in regions of the stellar atmosphere that are above the photosphere and dominated by magnetic heating, we expected to find correlations with less scatter between $\log R'_{HK}$ and $\log(L_{UV}/\log L_{bol})$ for each emission line. Figure 6 shows statistically significant correlations between $\log R'_{HK}$ and each of the normalized UV emission-line luminosities. The scatter about the $\log R'_{HK}$ best-fit lines is significantly smaller than for both $\log_{10}(L_{H\alpha}/L_{bol})$ and the $S$ index, except for N V, where the $\log_{10}(L_{H\alpha}/L_{bol})$ has a smaller scatter by 0.07 dex.

For each optical activity index, all of the individual UV lines' power-law slopes are consistent with each other within 1σ uncertainties. For $R'_{HK}$, $S$ index, and $\log_{10}(L_{H\alpha}/L_{bol})$, the weighted averages are, respectively, $1.57 \pm 0.06$, $1.89 \pm 0.07$, and $0.96 \pm 0.15$. The Mg II fit dominates the uncertainty in the $\log_{10}(L_{H\alpha}/L_{bol})$ average power-law slope. Excluding Mg II, the weighted average power-law slope for $\log_{10}(L_{H\alpha}/L_{bol})$ becomes $0.95 \pm 0.04$. We find no correlation between the power-law slope and line formation temperature for any of the fits. The Spearman correlation coefficient indicates a strong positive correlation with values for each UV emission line ranging between $0.76 \leqslant \rho \leqslant 0.85$. The probability of no correlation ($n$) is $<10^{-6}$ for each fit.
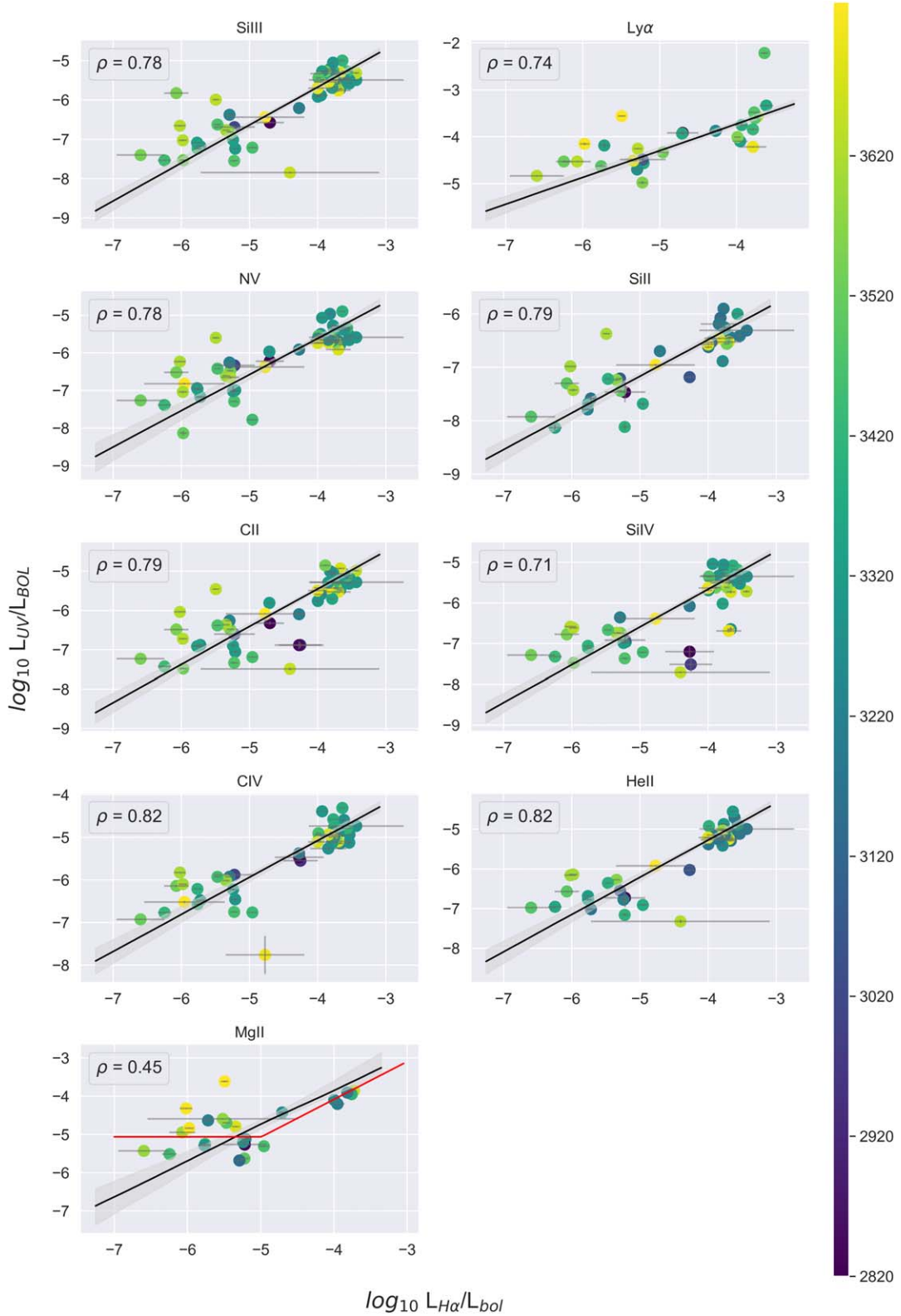
**Figure 4.** log $L_{\rm UV}$/log $L_{\rm Bol}$ as a function of $\log_{10} (L_{\rm H\alpha}/L_{\rm bol})$. Each circle represents a different stellar target from our sample color-coded by effective temperature. The log $L_{\rm UV}$/log $L_{\rm Bol}$ label on the $Y$-axis refers to the normalized UV luminosity of each individual emission line, and the luminosity errors are present but do not extend past the edges of each point. Calculated Spearman rank correlation coefficients ($\rho$) are shown for each graph. The black lines show the best fits (see Table 4 for parameters), and the gray shaded regions show the $1\sigma$ errors on the fits. In the Ly$\alpha$ subplot, the green point (LP 247-13) at $\log_{10} L_{\rm H\alpha}/L_{\rm bol} = -3.64 \pm 0.05$, $\log_{10} L$ (Ly$\alpha$)/$L_{\rm Bol} = -2.22 \pm 0.02$ is excluded from the fit. In the Mg II subplot, the yellow point (GJ 676 A) at $\log_{10} (L_{\rm H\alpha}/L_{\rm bol}) = -5.49 \pm 0.05$, $\log_{10} L$(Mg II)/ $L_{\rm Bol} = -3.62 \pm 0.02$ has been excluded from the black line fit, and we present an additional broken power-law fit (red line) that may better fit the data. Both fits are quantified and described further in Table 4. A version of this figure without the best fit lines and with the individual star names labeled is available.

**Table 4**
Fit Parameters for the $\log_{10}(L_{H\alpha}/L_{bol})$ Index and $\log_{10}(L_{UV}/L_{bol})$

| Transition name | $\alpha$ | $\beta$ | $\rho$ | $n$ | $\sigma$ |
|---|---|---|---|---|---|
| Si III | $0.99 \pm 0.07$ | $-1.66 \pm 0.32$ | 0.78 | <0.0001 | 0.53 |
| LyA[a] | $0.58 \pm 0.08$ | $-1.41 \pm 0.35$ | 0.74 | <0.0001 | 0.32 |
| N V | $1.02 \pm 0.11$ | $-1.44 \pm 0.48$ | 0.78 | <0.0001 | 0.55 |
| Si II | $0.77 \pm 0.11$ | $-3.29 \pm 0.50$ | 0.79 | <0.0001 | 0.42 |
| C II | $1.00 \pm 0.09$ | $-1.37 \pm 0.42$ | 0.79 | <0.0001 | 0.58 |
| Si IV | $0.95 \pm 0.08$ | $-1.85 \pm 0.34$ | 0.71 | <0.0001 | 0.60 |
| C IV | $0.91 \pm 0.07$ | $-1.38 \pm 0.32$ | 0.82 | <0.0001 | 0.50 |
| He II | $0.98 \pm 0.07$ | $-1.32 \pm 0.33$ | 0.82 | <0.0001 | 0.49 |
| Mg II[b,c] | $0.98 \pm 0.4$ | $0.17 \pm 2.1$ | 0.45 | 0.03 | 0.64 |

**Notes.** The scaling relations take the form $\log_{10} L_{UV} = (\alpha \times \log_{10}(L_{H\alpha}/L_{Bol})) + \beta$, where $L_{UV}$ represents each UV emission-line luminosity in erg s$^{-1}$. $\rho$ is the Spearman correlation coefficient, $n$ is the probability of no correlation, and $\sigma$ is the standard deviation of the data points about the best-fit line (dex).
[a] LP 247-13 was not included in the fit because it is a significant outlier with a very small relative error on $L(Ly\alpha)/L_{Bol}$.
[b] Fit with a double Gaussian because wings cannot be resolved at the lower S/N of these blended emission lines.
[c] Fluxes uniformly corrected for $30\% \pm 10\%$ ISM absorption (see Section 3 and Youngblood et al. 2016). The fit does not include the significant outlier GJ676A. To account for scatter in the inactive range of the plot, we also fit a broken power law with a crossover point at $\log_{10}(L_{H\alpha}/L_{Bol}) = -5.0$, separating the active and inactive regimes. The inactive regime is described by $\log_{10}(L_{UV}/L_{bol}) = -5.06 \pm 0.01$, and the active regime by $\log_{10}(L_{UV}/L_{bol}) = (0.99 \pm 0.20) \times \log_{10}(L_{H\alpha}/L_{bol}) - 0.14 \pm 0.82$.

The standard deviations about the best-fit lines are $0.31 \leqslant \sigma \leqslant 0.61$ dex. Comparing these parameters to Youngblood et al. (2017), we see that our standard deviations about the best fit are generally larger, indicating more scatter. This is likely due to our larger and more diverse sample of stars in addition to using a different Ca II activity indicator ($\log R'_{HK}$). Additionally, we analyzed the relationship between the residuals around our $\log R'_{HK}$ best fit for each UV line and stellar effective temperature and found a shallow, statistically significant negative correlation. This indicates that the hotter stars' UV luminosities are generally overpredicted by the best-fit line and cooler stars are generally underpredicted.

### 3.1. Outliers

Despite a tight relation between $R'_{HK}$ and $\log L_{UV}/\log L_{Bol}$ across three orders of magnitude of $\log L_{UV}/\log L_{Bol}$ values in our sample of M dwarfs, some stars are not well fit by the established trends. These include GJ 849, GJ 3290, GJ 876, LP 247-13, 2MASS J23261069–7323498, and GJ 676 A. Almost all of these stars are outliers in the sense that their normalized UV line luminosity is much higher than other stars of a similar $R'_{HK}$ value, except for 2MASS J23261069–7323498. We have examined all of these stars' spectra for flares and found none that could explain such a large discrepancy from their neighbors. GJ 876 (M4V; $P_{rot} = 96.7$ days; Rivera et al. 2005) was noted as a UV-bright outlier in Youngblood et al. (2017) and had many strong flares (Youngblood et al. 2017; Loyd et al. 2018b). While we do not think that large flares are affecting the UV line measurements, they are indicative of an elevated activity that may manifest itself in other ways, such as the quiescent UV luminosity. LP 247-13 is a young M3 dwarf and a potential member of the $\sim 625$ Myr old Hyades cluster, although Shkolnik et al. (2012) note that its low surface gravity indicates it could be much younger. This star is one

of the most UV-bright members of our sample, and in particular, its $L(Ly\alpha)/L_{bol}$ is an order of magnitude greater than the next brightest star. LP 247-13 significantly drives the slope of the $Ly\alpha$–$R'_{HK}$ correlation to a steeper value, and was removed from the $Ly\alpha$–$H\alpha$ fit for its extreme effect on that best-fit line. More details about LP 247-13 can be found in upcoming publications about the FUMES survey (J. S. Pineda et al. 2020, in preparation and A. Youngblood et al. 2020, in preparation). Similarly, GJ 3290 and 2MASS J23261069–7323498 are both young stars (625 Myr and 40 Myr, approximately) and will be discussed in an upcoming publication about the HAZMAT survey (R. O. P. Loyd et al. 2020, in preparation). GJ 849 and GJ 676 A are both field-age stars and will be discussed in upcoming publications about the Mega-MUSCLES survey.

Here we discuss the impact of stellar variability on the general scatter in our correlations. None of our targets' optical and UV spectra were taken simultaneously, and the time between the spectra span days to years. M dwarfs exhibit activity-related variability in UV and optical emission lines on many timescales including minutes (flares; Baliunas & Raymond 1984; Hilton et al. 2010; Loyd et al. 2018b), days to months (rotational modulation and the emergence and decay of active regions and starspots; Vaughan et al. 1981; Suárez Mascareño et al. 2015), and years (magnetic activity cycles; Gomes da Silva et al. 2012; Robertson et al. 2013; Buccino et al. 2014; Toledo-Padrón et al. 2019). Mitigating the effect of rotation and stellar cycles through modeling a baseline for the sample is a promising topic for future work. It would also be interesting but extremely challenging to gather a truly simultaneous UV + optical data set to remove the scattering effect of stellar variability within individual stars from UV–optical correlations.

We have removed the effects of large flares by visually inspecting our optical spectra and removing spectra exhibiting obvious flaring (significantly brighter emission lines and/or continuum enhancement). We inspected the UV light curves of outliers for flares, and we did not find any that could have increased the UV line luminosity by a factor of 2 (0.3 dex) or more. Typically, integration times in the UV are $\gtrsim 1$ hour long to build up sufficient S/N, and brief flares do not greatly affect the cumulative spectrum (Loyd et al. 2018b, 2018a). Our significant outliers (listed above) have UV line luminosities that are $>1$ dex above or below the best-fit line, which is not explained by flares. However, at least some of the scatter in our correlations must be due to flares as we were unable to discern small flares in our spectra.

Almost all of our optical and UV data were taken nonsimultaneously, which means that our results are susceptible to rotational and activity cycle effects that occur on $>1$ day timescales. This affects our UV spectra the most as almost all of our targets had their UV data taken in a single day, whereas many of our targets' optical spectra were taken over multiple epochs spread over years and decades. Thus, the optical spectral variability over rotational and activity time-scales should be averaged out. Assuming the rotational and cycle variability of M dwarfs is similar to the Sun's, the amplitude of variations is significantly larger in the UV than in the optical. Based on SORCE solar spectral irradiance time-series data[28] (McClintock et al. 2005), the Sun varies on 27 day (rotational) timescales by 1%–5% at solar minimum and 10%–30% at solar maximum in UV lines like C II, N V, and Ly$\alpha$, although Ly$\alpha$ can vary by as little as 5% during solar
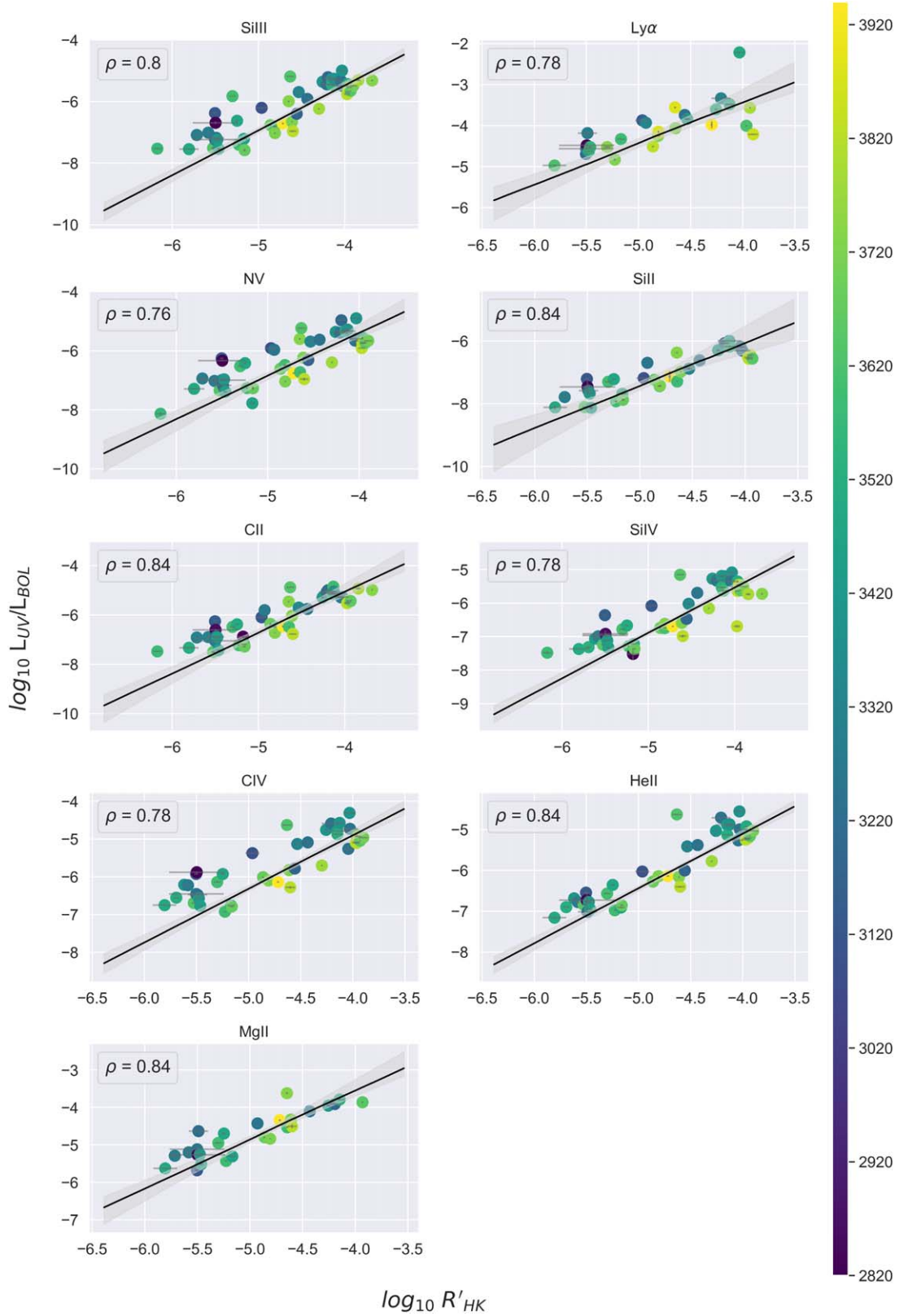
---

[28] https://lasp.colorado.edu/lisird/
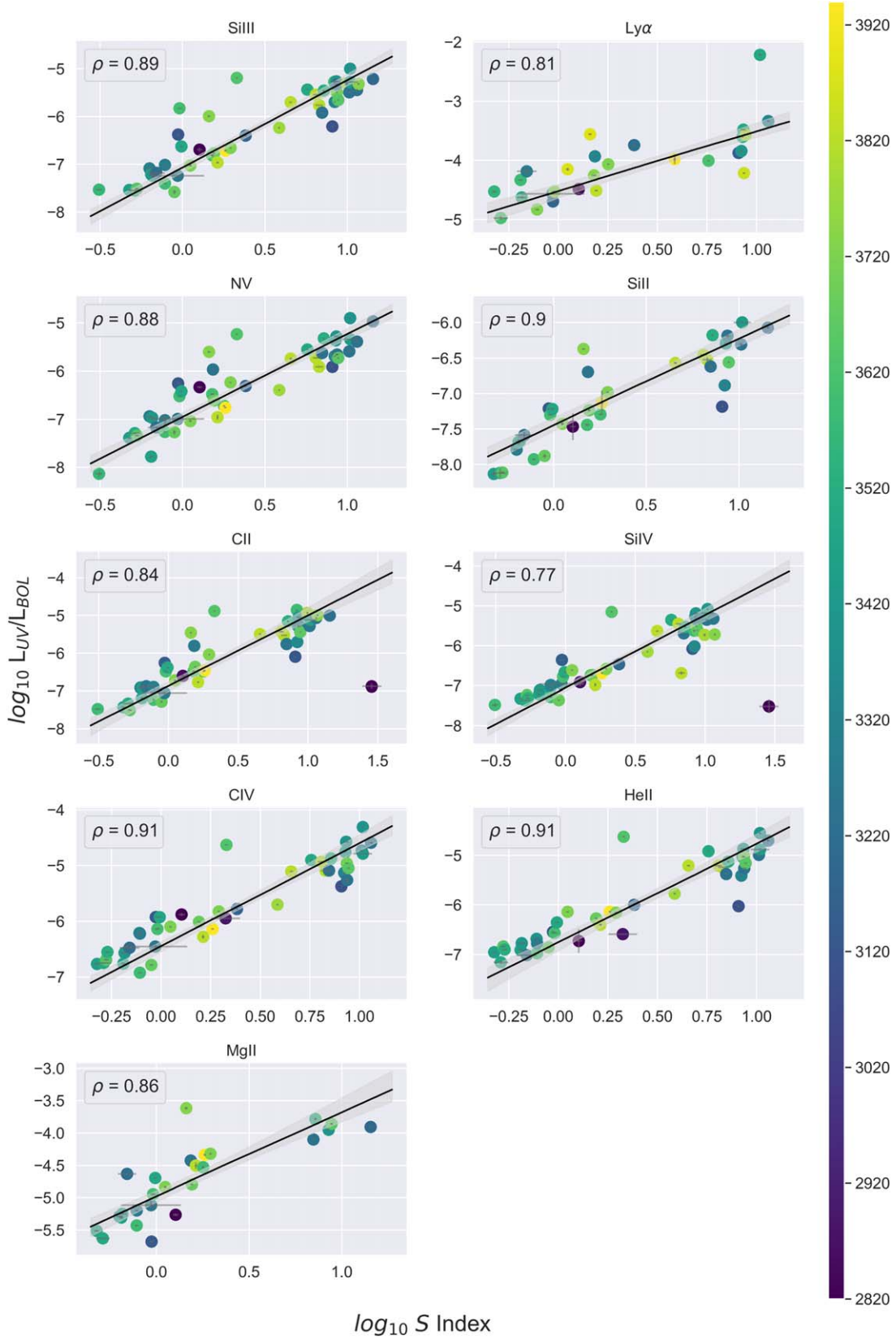
**Figure 5.** Same as Figure 4 for log ($L_{UV}$/log $L_{bol}$) as a function of the Ca II $S$ index. A version of this figure without the best-fit lines and with the individual star names labeled is available.

maximum. Over the course of the 11 yr solar cycle, the same lines modulate by ∼30%, although Lyα can modulate by as much as 50%. Conversely, the Sun's $S$-index and $R'_{HK}$ values

vary on an 11 yr timescale from log $S = -0.80$ to $-0.74$ and log $R'_{HK} = -4.98$ to $-4.91$, or ∼15% (0.06–0.07 dex; Egeland et al. 2017). This variation is much smaller than the error bars

**Figure 6.** Same as Figure 4 for $\log L_{\mathrm{UV}}/\log L_{\mathrm{Bol}}$ as a function of the Ca II $R'_{\mathrm{HK}}$ index. A version of this figure without the best-fit lines and with the individual star names labeled is available.

on our measurements. M dwarf activity cycles have been detected in the UV for GJ 551 (Proxima Centauri); Wargelin et al. (2017) found ~10% amplitude variations in the broadband Neil Gehrels Swift Observatory's UVW1 (NUV) filter over several years. Tracing M dwarf cycles in the optical is more common, with 2%–3% fluctuations observed in

**Table 5**
Fit Parameters for $\log_{10} S$ and $\log_{10}(L_{\mathrm{UV}}/L_{\mathrm{bol}})$

| Transition name | $\alpha$ | $\beta$ | $\rho$ | $n$ | $\sigma$ |
|---|---|---|---|---|---|
| Si III | $1.84 \pm 0.17$ | $-7.07 \pm 0.12$ | 0.89 | <0.0001 | 0.39 |
| LyA | $1.05 \pm 0.19$ | $-4.53 \pm 0.13$ | 0.81 | <0.0001 | 0.39 |
| N V | $1.73 \pm 0.17$ | $-6.96 \pm 0.12$ | 0.88 | <0.0001 | 0.39 |
| Si II | $1.22 \pm 0.16$ | $-7.43 \pm 0.10$ | 0.90 | <0.0001 | 0.31 |
| C II | $1.91 \pm 0.22$ | $-6.89 \pm 0.14$ | 0.84 | <0.0001 | 0.59 |
| Si IV | $1.84 \pm 0.17$ | $-7.06 \pm 0.11$ | 0.77 | <0.0001 | 0.61 |
| C IV | $1.87 \pm 0.16$ | $-6.45 \pm 0.11$ | 0.91 | <0.0001 | 0.35 |
| He II | $2.04 \pm 0.22$ | $-6.78 \pm 0.15$ | 0.91 | <0.0001 | 0.41 |
| Mg II[a,b] | $1.35 \pm 0.16$ | $-4.98 \pm 0.08$ | 0.86 | <0.0001 | 0.37 |

**Notes.** The scaling relations take the form $\log_{10} L_{\mathrm{UV}} = (\alpha \times \log_{10} S) + \beta$, where $L_{\mathrm{UV}}$ represents each UV emission-line luminosity in erg s$^{-1}$. $\rho$ is the Spearman correlation coefficient, $n$ is the probability of no correlation, and $\sigma$ is the standard deviation of the data points about the best-fit line (dex).
[a] Fit with a double Gaussian because wings cannot be resolved at the lower S/N of these blended emission lines.
[b] Fluxes uniformly corrected for 30% ± 10% ISM absorption (see Section 3 and Youngblood et al. 2016).

H$\alpha$ intensity (Robertson et al. 2013) and 10%–30% fluctuations observed in Ca II H&K intensity (Buccino et al. 2014; Toledo-Padrón et al. 2019).

## 4. Discussion

Are our presented UV–optical scaling relations precise enough for photochemical and atmospheric escape models of exoplanets? In this section, we analyze the expected UV precision for a range of typical $\log_{10} R'_{\mathrm{HK}}$ values and measurement precisions. We focus on $R'_{\mathrm{HK}}$ because those relations had the least scatter. Using a star with $\log_{10} R'_{\mathrm{HK}} = -4.5 \pm 0.30$ (~7% uncertainty) as an example, the precision of our UV luminosity estimates ($\sigma_L/L$) for each emission line ranges from factors of 2.27–4.65 (0.36–0.67 dex), depending on the specific emission line. We evaluated this precision by comparing the calculated error and the predicted average luminosity value. The uncertainties of each predicted UV emission-line luminosity are dominated by the error of the best-fit line intercept and the error on $\log_{10} R'_{\mathrm{HK}}$. From the standard deviations about the best-fit lines (Table 3), we estimate that using our scaling relations allows one to approximate the individual $L_{\mathrm{UV}}/L_{\mathrm{bol}}$ of the nine UV emission lines examined in this work within a factor of ~2–4 (0.31–0.61 dex) for a typical M dwarf UV spectrum. Underscoring the utility and impact of these correlations is the fact that the parameter space for the $L_{\mathrm{UV}}/L_{\mathrm{bol}}$ of our target stars spans almost three orders of magnitude.

Rugheimer et al. (2015) examined the effect of variations in UV spectra on modeled exoplanet spectra and found that a factor of $\lesssim$10 UV flux variations propagate to 10%–30% level changes in the depths of spectral features from simulated directly imaged Earth-like planets. Depending on the precision of observed reflection spectra, using our $R'_{\mathrm{HK}}$ scaling relations could be suitable for photochemical modeling purposes. For determining atmospheric escape rates from exoplanets, obtaining accurate EUV fluxes of M dwarfs is notoriously challenging due to a dearth of EUV spectra, and much of the exoplanet community relies on scaling relations between the EUV and other spectral regions like the FUV and X-ray (Sanz-Forcada et al. 2011; Linsky et al. 2013; Chadney et al. 2015; France et al. 2018). For some exoplanets needing atmospheric escape modeling, only an optical

spectrum of the host star may be available, and here we estimate the suitability of our optical–FUV scaling relations for extrapolating to the EUV. Bolmont et al. (2017) showed that in the low- and high-EUV flux regimes, water-loss rates on an Earth-like planet orbiting TRAPPIST-1 increase at the same rate as EUV flux. However, in the moderate EUV flux regime, water-loss rates increase more slowly than a 1:1 relation with increasing EUV flux, indicating that uncertainties in the incident EUV flux up to a factor of 10 may be acceptable in this regime. However, determining where this moderate EUV regime is may depend on the particular star and simulated planet. Thus, it is unlikely that our optical–FUV scaling relations can be propagated into other FUV–EUV scaling relations (e.g., Linsky et al. 2013; France et al. 2018) and retain a sufficiently small level of uncertainty that would not dominate over the escape model's uncertainties. Based on these examples of models that consider the impact of absolute UV flux on exoplanets, we conclude that the precision provided by this work's scaling relations may be sufficient for photochemical modeling needs, but not atmospheric escape modeling. Further work is needed to demonstrate the impact of UV spectrum uncertainties on photochemical models, and will be addressed in an upcoming paper (D. J. Teal et al. 2020, in preparation).

Ly$\alpha$ alone represents 75%–90% of the 1200–1700 Å flux for typical M dwarfs (e.g., GJ 832, GJ 876, GJ 176; France et al. 2013), so by estimating (or directly measuring and reconstructing) the Ly$\alpha$ line, one can account for the majority of the FUV flux from an M dwarf. However, not accounting for the remaining SED across the FUV might significantly change results from photochemical models given the strong wavelength dependence of photoabsorption cross sections of key atmospheric molecules. Here we estimate the percentage of non-Ly$\alpha$ FUV flux made up by the seven FUV lines[29] (excluding Ly$\alpha$) we analyzed (Si II, Si III, Si IV, C II, C IV, He II, N V). An important limitation in our ability to characterize the FUV spectra of M dwarfs is the extremely faint FUV continuum (photospheric and chromospheric), which is well below the COS and STIS instrument background levels in almost all cases. Loyd et al. (2016) detected weak FUV continuum emission in three of seven of the MUSCLES M dwarfs (GJ 832, GJ 876, GJ 176) by integrating across multiple line-free bandpasses and estimated that the continuum emission comprises at least 10% of the 1307–1700 Å FUV flux region. D. Tilipman et al. (2020, in preparation) created high-resolution synthetic FUV spectra of GJ 832 and GJ 581 and found that the percentage of FUV emission between 1300 and 1700 Å comprised by continuum is 57% and 43%, respectively. Our ability to develop scaling relations for estimating the FUV continuum of M dwarfs depends on more sensitive observations of these stars as well as model stellar atmospheres that accurately treat the upper atmosphere (Fontenla et al. 2016; Peacock et al. 2019; D. Tilipman et al. 2020, in preparation). Linsky et al. (2012) showed significant correlations between the FUV continuum of G dwarfs (measured over 1382–1392 Å) and stellar rotation period as well as Si IV flux, so similar correlations likely exist for M dwarfs.

By measuring the mean flux density in two line-free regions (1337–1351 Å and 1374–1392 Å) from our spectra of GJ 832, GJ 876, and GJ 176, we estimate that weak FUV emission lines and continuum comprise 20%–50% of the non-Ly$\alpha$ 1200–1700 Å flux, while our seven FUV lines (excluding Ly$\alpha$) comprise 30%–50%. Other weak-to-moderate intensity emission lines that we did not include in our study comprise any remaining

---

[29] Note that Mg II is an NUV doublet and is not included in the FUV analysis.
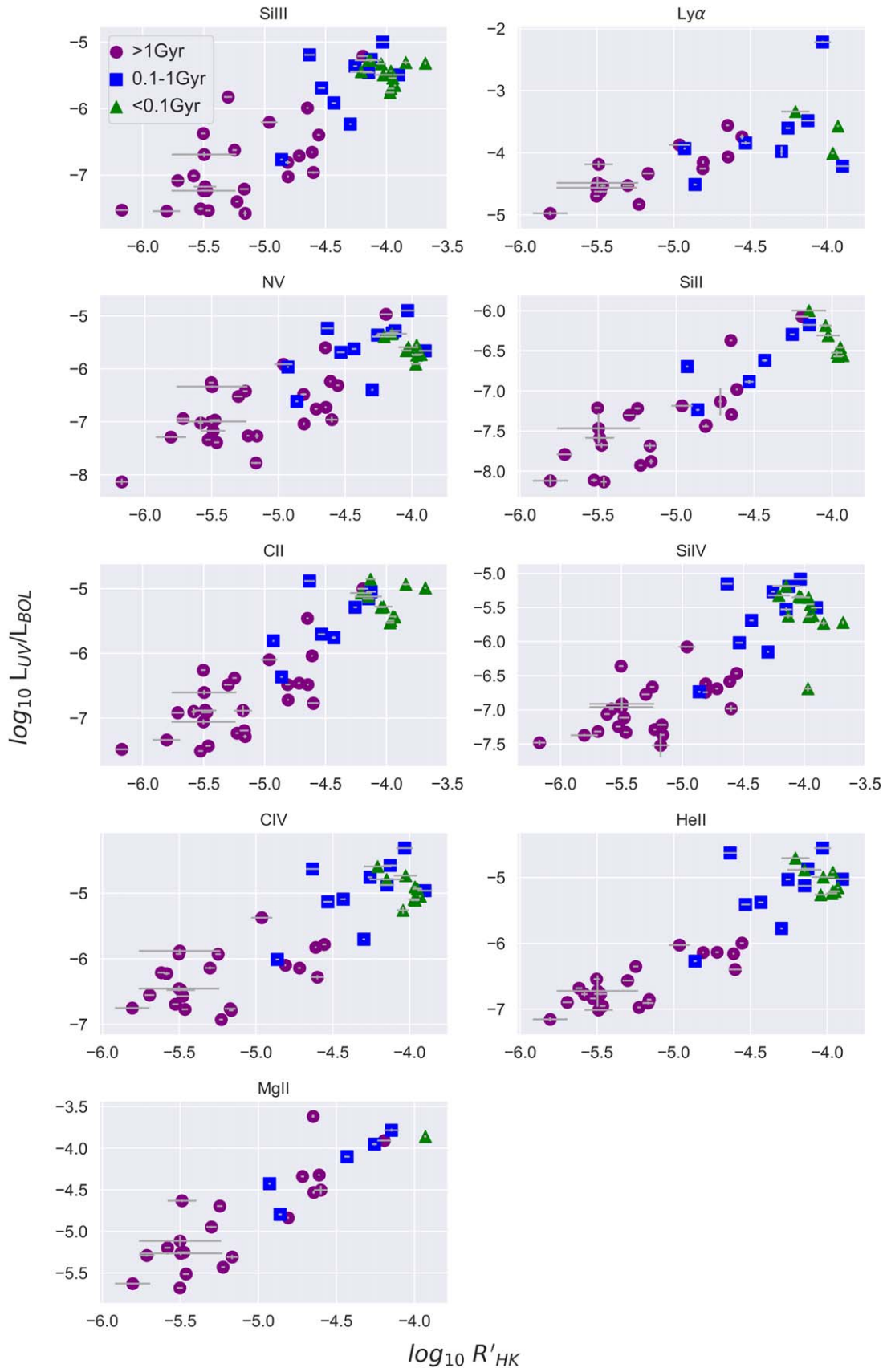
**Figure 7.** Same as Figure 6 with color breakdown according to stellar age. Purple circles show the >1 Gyr (or field-age) population, the blue squares show the 0.1–1 Gyr intermediate-age population, and the green triangles show the young <0.1 Gyr (<100 Myr) population.
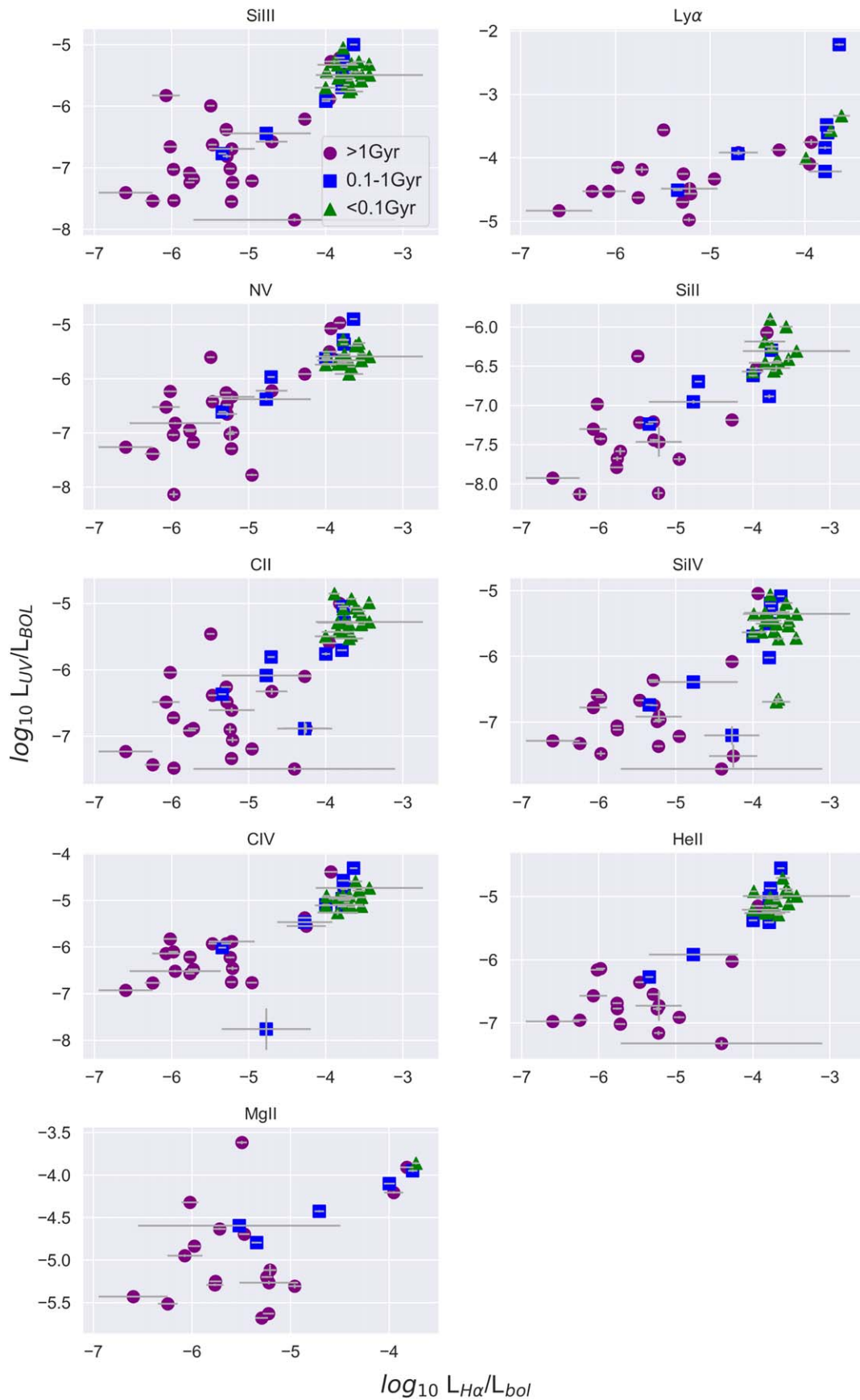
**Figure 8.** Same as Figure 4 with color breakdown according to stellar age. Purple circles show the >1 Gyr (or field-age) population, the blue squares show the 0.1–1 Gyr intermediate-age population, and the green triangles show the young <0.1 Gyr (<100 Myr) population.
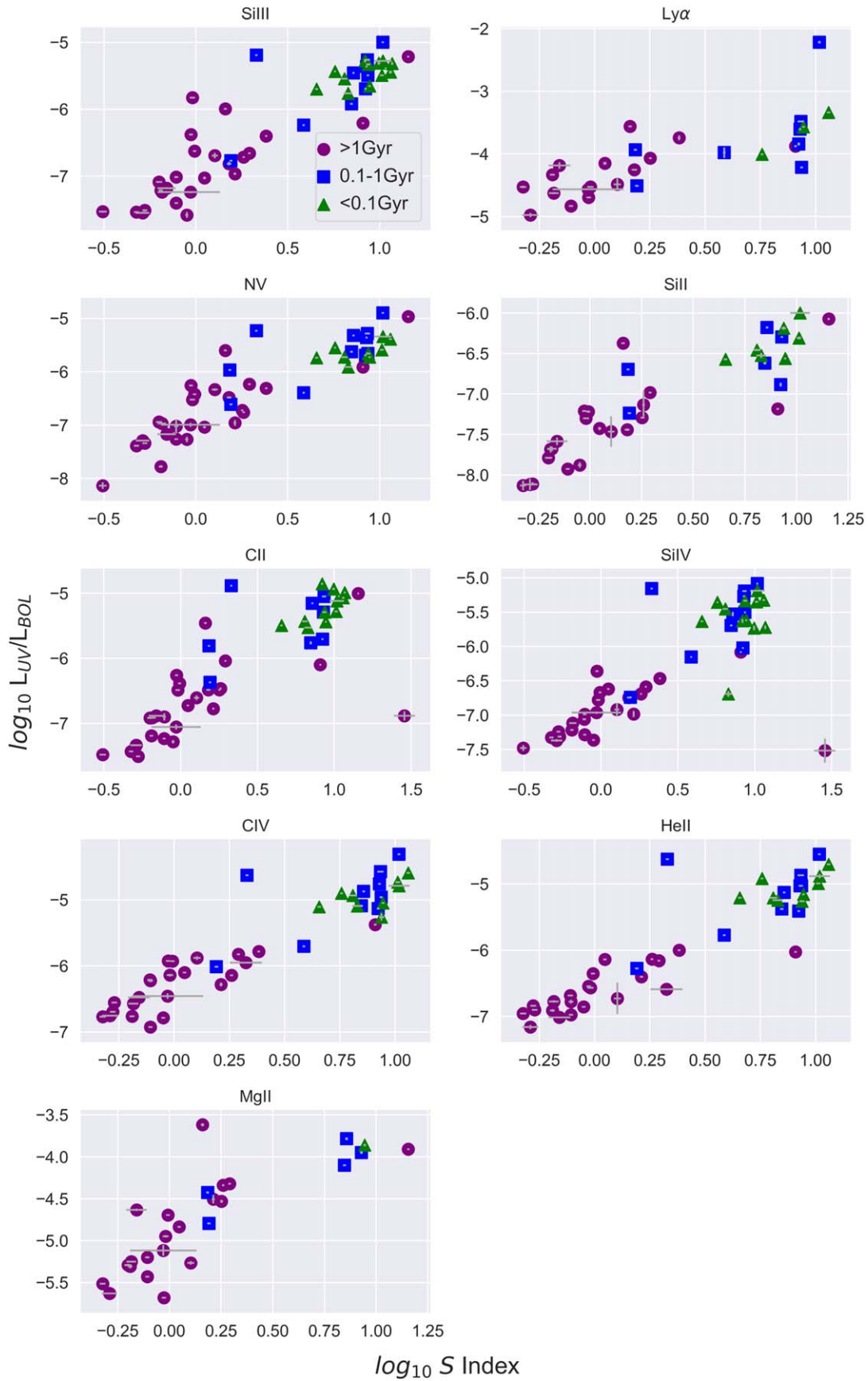
**Figure 9.** Same as Figure 5 with color breakdown according to stellar age. Purple circles show the >1 Gyr (or field-age) population, the blue squares show the 0.1–1 Gyr intermediate-age population, and the green triangles show the young <0.1 Gyr (<100 Myr) population.

flux. This means that 50%–70% of the non-Ly$\alpha$ FUV flux is unaccounted for by our scaling relations. A direct FUV spectrum may be best to accurately characterize the $1200 - 1210 + 1222 - 1700$ Å FUV flux. However, if the weak forest of emission lines and FUV continuum is below the detector sensitivity, as is the case for essentially all but the brightest M dwarfs observable with HST, using the scaling relations to scale a high-S/N M dwarf spectrum could be an appropriate substitute for a direct FUV spectrum with HST. Similarly, our scaling relations do not account for flux from faint emission lines in the NUV or any chromospheric continuum. In the NUV, Mg II at 2796, 2802 Å is by far the brightest emission line, but there is a forest of much fainter Fe II lines as well as other atomic species that can be difficult to measure with HST depending on the brightness of the target. More work is needed to assess the impact of excluding faint but numerous emission lines from UV spectral inputs on photochemical models of exoplanet atmospheres.

We also examine whether the scaling relations change based on the stellar age given that magnetic dynamos, which are ultimately responsible for the presence of these emission lines, change over a star's lifetime. We subdivided each plot of $R'_{HK}$, $S$ index, and $\log_{10} L_{H\alpha}/L_{bol}$ as a function of UV activity into groups of stars <0.1, 0.1–1 Gyr (inclusive), and >1 Gyr as shown in Figures 7–9. As expected, the oldest stars are typically the least active and the youngest are usually the most active. The youngest stars are clumped in the high activity region of the plots with no apparent linear relationship between optical and UV activity, whereas the intermediate- and field-age stars span a range of activity levels. We note that we have no stars in our sample with $\log_{10} R'_{HK}$ values $>-3.8$, which align with the finding in Astudillo-Defru et al. (2016) that activity saturates around $\log_{10} R'_{HK} = -3.5$. Stelzer et al. (2013), Shkolnik & Barman (2014), and France et al. (2018) demonstrated a similar saturation limit with UV luminosity, although this limit varies depending on the emission line. We conclude that these young stars are saturated or nearly saturated in UV and Ca II luminosity, which explains the lack of correlation among them. However, we expect that a similarly narrow range of emission strength for older stars would also show a lack of correlation.

## 5. Summary

We have extended and improved upon previous efforts to determine useful scaling relations between the optical and UV spectra of M dwarfs. Through empirical analysis of four standard optical activity indices (H$\alpha$ EW and $\log_{10} (L_{H\alpha}/L_{bol})$, Ca II $S$ index, and $R'_{HK}$), we have determined a new method of estimating the UV luminosity of M dwarfs when UV data are not available. The main findings are outlined below.

1. Time-averaged $R'_{HK}$, $S$ index, and $\log_{10} (L_{H\alpha}/L_{bol})$ correlate positively and significantly with the normalized UV luminosity ($L_{UV}/L_{bol}$) of nine far- and near-UV spectral lines (see Tables 3–5). The scatter about the best-fit lines is lowest for $R'_{HK}$ (0.31–0.61 dex) and highest for the $S$ index (0.58–0.84 dex). The scatter around the $\log_{10} (L_{H\alpha}/L_{bol})$ best fit lines ranges from 0.42–0.68 dex, excluding Mg II. No statistically significant correlation was found between $L_{UV}/L_{bol}$ and H$\alpha$ EW.
2. The luminosity of individual UV emission lines normalized to stellar bolometric luminosity can be estimated with $R'_{HK}$ within a factor of $\sim$2–4 (0.31–0.61 dex; Table 3). This

implies that the scaling relations defined in this study can be a useful substitute for direct UV observations of M dwarfs.

The results presented here address important problems in the characterization of cool ($T_{eq} \lesssim 1000$ K) exoplanets and the search for habitable exoplanets. M dwarfs are excellent targets for finding and characterizing small and/or cool exoplanets. However, their UV spectra can have significant and misleading effects on the composition of exoplanet atmospheres. The UV–$R'_{HK}$ scaling relation developed in this paper provides an alternative method for completing photochemical analysis of exoplanet atmospheres without needing observations from space-based telescopes with valuable and limited resources. This will allow for efficient follow-up on exoplanet discoveries, which is essential given the number of current and upcoming dedicated exoplanet missions. In addition, this work will help determine which planets may be the most amenable for further study so that the outcome of observations on major missions like JWST can be maximized.

Data were graciously made available through the ESO archive from the following ESO programs: 072.C-0488(E), 183.C-0437(A), 198.C-0838(A), 077.C-0364(E), 191.C-0873 (D), 191.C-0873(B), 191.C-0873(A), 082.C-0718(B), 183.C-0972(A), 085.C-0019(A), 091.C-0034(A), 090.C-0421(A), 191.C-0873(F), 191.C-0873(E), 095.C-0718(A), 192.C-0224 (A), 191.C-0505(A), 192.C-0224(H), 192.C-0224(B), 089.C-0904(A), 095.D-0291(A), 088.C-0506(A), 095.C-0437(A), 082.C-0218(A), 180.C-0886(A), 093.C-0343(A), 076.C-0010 (A), 074.C-0037(A), 60.A-9036(A), 192.C-0224(G), 192.C-0224(C), 096.C-0876(A), 097.C-0390(B), 099.C-0225(A), 68. D-0166(A), 075.C-0202(A), 099.C-0205(A), 075.C-0321(A), 082.D-0953(A), 099.C-0880(A), 096.C-0258(A), 089.C-0207 (A), 077.C-0012(A), 079.C-0046(A), 080.D-0151(A), 276.C-5054(A), 086.D-0062(A), 081.D-0190(A), 089.C-0732(A), 093.C-0409(A), 095.C-0551(A), 096.C-0460(A), 092.C-0721 (A), 192.C-0852(M), 098.C-0366(A), 088.C-0662(B), 089.C-0497(A), 076.C-0155(A), 495.L-0963(A), 074.B-0639(A).

## ORCID iDs

Katherine Melbourne ⑩ https://orcid.org/0000-0002-8423-6904
Allison Youngblood ⑩ https://orcid.org/0000-0002-1176-3391
Kevin France ⑩ https://orcid.org/0000-0002-1002-3674
C. S. Froning ⑩ https://orcid.org/0000-0001-8499-2892
J. Sebastian Pineda ⑩ https://orcid.org/0000-0002-4489-0135
Evgenya L. Shkolnik ⑩ https://orcid.org/0000-0002-7260-5821
David J. Wilson ⑩ https://orcid.org/0000-0001-9667-9449
Brian E. Wood ⑩ https://orcid.org/0000-0002-4998-0893
Sarbani Basu ⑩ https://orcid.org/0000-0002-6163-3472
Aki Roberge ⑩ https://orcid.org/0000-0002-2989-3725
Joshua E. Schlieder ⑩ https://orcid.org/0000-0001-5347-7062
P. Wilson Cauley ⑩ https://orcid.org/0000-0001-9207-0564
R. O. Parke Loyd ⑩ https://orcid.org/0000-0001-5646-6668
Elisabeth R. Newton ⑩ https://orcid.org/0000-0003-4150-841X
Adam Schneider ⑩ https://orcid.org/0000-0002-6294-5937
Nicole Arulanantham ⑩ https://orcid.org/0000-0003-2631-5265
Zachory Berta-Thompson ⑩ https://orcid.org/0000-0002-3321-4924
Alexander Brown ⑩ https://orcid.org/0000-0003-2631-3905
Eliza Kempton ⑩ https://orcid.org/0000-0002-1337-9051
Jeffrey L. Linsky ⑩ https://orcid.org/0000-0003-4446-3181
Sarah E. Logsdon ⑩ https://orcid.org/0000-0002-9632-9382
Pablo Mauas ⑩ https://orcid.org/0000-0003-0873-0262
Isabella Pagano ⑩ https://orcid.org/0000-0001-9573-4928
Sarah Peacock ⑩ https://orcid.org/0000-0002-1046-025X
Seth Redfield ⑩ https://orcid.org/0000-0003-3786-3486
Sarah Rugheimer ⑩ https://orcid.org/0000-0003-1620-7658
P. Christian Schneider ⑩ https://orcid.org/0000-0002-5094-2245
D. J. Teal ⑩ https://orcid.org/0000-0002-1912-3057
Feng Tian ⑩ https://orcid.org/0000-0002-9607-560X
Dennis Tilipman ⑩ https://orcid.org/0000-0001-9361-6629
Mariela Vieytes ⑩ https://orcid.org/0000-0003-4615-8746

## References

Allard, F., Homeier, D., & Freytag, B. 2012, RSPTA, 370, 2765
Alonso-Floriano, F. J., Morales, J. C., Caballero, J. A., et al. 2015, A&A, 577, 128
Anglada-Escude, G., Arriagada, P., Tuomi, M., et al. 2014, MNRAS, 443, L89
Anglada-Escudé, G., & Tuomi, M. 2012, A&A, 548, A58
Arney, G., Domagal-Goldman, S. D., & Meadows, V. S. 2018, AsBio, 18, 311
Arney, G. N., Meadows, V. S., Domagal-Goldman, S. D., et al. 2017, ApJ, 836, 49
Astudillo-Defru, N., Delfosse, X., Bonfils, X., et al. 2016, A&A, 600, 13
Astudillo-Defru, N., Delfosse, X., Bonfils, X., et al. 2017, A&A, 600, A13
Awiphan, S., Kerins, E., Pichadee, S., et al. 2016, MNRAS, 463, 2574
Ayres, T. R. 2010, ApJS, 187, 149
Baliunas, S. L., & Raymond, J. C. 1984, ApJ, 282, 728
Batalha, N. M., Rowe, J. F., Bryson, S. T., et al. 2013, ApJS, 204, 24
Bazot, M., Christensen-Dalsgaard, J., Gizon, L., & Benomar, O. 2016, MNRAS, 460, 1254
Bell, C. P. M., Mamajek, E. E., & Naylor, T. 2015, MNRAS, 454, 593
Berta, Z. K., Charbonneau, D., Bean, J., et al. 2011, ApJ, 736, 12
Berta-Thompson, Z. K., Irwin, J., Charbonneau, D., et al. 2015, Natur, 527, 204
Beuermann, K., Baraffe, I., & Hauschildt, P. 1999, A&A, 348, 524
Biddle, L. I., Pearson, K. A., Crossfield, I. J. M., et al. 2014, MNRAS, 443, 1810
Bochanski, J. J., Hawley, S. L., Covey, K. R., et al. 2010, AJ, 139, 2679
Bolmont, E., Selsis, F., Owen, J. E., et al. 2017, MNRAS, 464, 3728
Bonfils, X., Delfosse, X., Udry, S., et al. 2013, A&A, 549, 109
Bonfils, X., Forveille, T., Delfosse, X., et al. 2005, A&A, 443, L15
Bourrier, V., Lecavelier des Etangs, A., Ehrenreich, D., et al. 2018, A&A, 620, A147
Buccino, A. P., Petrucci, R., Jofré, E., & Mauas, P. J. D. 2014, ApJL, 781, L9
Burgasser, A. J., & Mamajek, E. E. 2017, ApJ, 845, 110
Butler, R. P., Johnson, J. A., Marcy, G. W., et al. 2006, PASP, 118, 1685
Caffau, E., Ludwig, H. G., Bonifacio, P., et al. 2010, A&A, 514, A92
Chadney, J. M., Galand, M., Unruh, Y. C., Koskinen, T. T., & Sanz-Forcada, J. 2015, Icar, 250, 357
Cincunegui, C., Díaz, R. F., & Mauas, P. J. D. 2007a, A&A, 461, 1107
Cincunegui, C., Díaz, R. F., & Mauas, P. J. D. 2007b, A&A, 469, 309
Costa, E., Méndez, R. A., Jao, W. C., et al. 2005, AJ, 130, 337
Costa, E., Méndez, R. A., Jao, W. C., et al. 2006, AJ, 132, 1234
Cram, L. E., & Mullan, D. J. 1985, ApJ, 294, 626
Crossfield, I. J. M., & Kreidberg, L. 2017, AJ, 154, 261
Cruz, K. L., Reid, I. N., Liebert, J., Kirkpatrick, J. D., & Lowrance, P. J. 2003, AJ, 126, 2421
Cutri, R. M., Skrutskie, M. F., van Dyk, S., et al. 2003, yCat, 2246, 0
D'Antona, F. 1986, MmSAI, 57, 317
Davison, C. L., White, R. J., Henry, T. J., et al. 2015, AJ, 149, 106
Dekker, H., D'Odorico, S., Kaufer, A., Delabre, B., & Kotzlowski, H. 2000, Proc. SPIE, 4008, 534
Delfosse, X., Forveille, T., Perrier, C., & Mayor, M. 1998, A&A, 331, 581
Demory, B. O., Ségransan, D., Forveille, T., et al. 2009, A&A, 505, 205
Dere, K. P., Landi, E., Mason, H. E., Monsignori Fossi, B. C., & Young, P. R. 1997, A&AS, 125, 149
Domagal-Goldman, S. D., Segura, A., Claire, M. W., Robinson, T. D., & Meadows, V. S. 2014, ApJ, 792, 90
Douglas, S. T., Agüeros, M. A., Covey, K. R., et al. 2014, ApJ, 795, 161
Dreizler, S., Jeffers, S. V., Rodríguez, E., et al. 2020, MNRAS, 493, 536
Dressing, C. D., & Charbonneau, D. 2015, ApJ, 807, 45
Dressing, C. D., Sinukoff, E., Fulton, B. J., et al. 2018, AJ, 156, 70
Dressing, C. D., Vanderburg, A., Schlieder, J. E., et al. 2017, AJ, 154, 207
Ducati, J. R. 2002, yCat, 37, 0
Egeland, R., Soon, W., Baliunas, S., et al. 2017, ApJ, 835, 25
Finch, C. T., Zacharias, N., Subasavage, J. P., Henry, T. J., & Riedel, A. R. 2014, AJ, 148, 119
Fontenla, J. M., Linsky, J. L., Witbrod, J., et al. 2016, ApJ, 830, 154
Fossati, L., Marcelja, S. E., Staab, D., et al. 2017, A&A, 601, A104
France, K., Arulanantham, N., Fossati, L., et al. 2018, ApJS, 239, 16
France, K., Froning, C. S., Linsky, J. L., et al. 2013, ApJ, 763, 149
France, K., Loyd, R. O. P., Youngblood, A., et al. 2016, ApJ, 820, 89
France, K., Schindhelm, E., Herczeg, G. J., et al. 2012, ApJ, 756, 171
Froning, C. S., Kowalski, A., France, K., et al. 2019, ApJL, 871, L26
Gagné, J., & Faherty, J. K. 2018, ApJ, 862, 138
Gaia Collaboration, Brown, A. G. A., Vallenari, A., et al. 2018, A&A, 616, A1
Gaidos, E., Mann, A. W., Lépine, S., et al. 2014, MNRAS, 443, 2561
Gao, P., Hu, R., Robinson, T. D., Li, C., & Yung, Y. L. 2015, ApJ, 806, 249

Gizis, J. E. 1997, AJ, 113, 806

Gizis, J. E., Reid, I. N., & Hawley, S. L. 2002, AJ, 123, 3356

Gomes da Silva, J., Santos, N. C., Bonfils, X., et al. 2012, A&A, 541, A9

Guinan, E. F., Engle, S. G., & Durbin, A. 2016, ApJ, 821, 81

Hall, J. C., Lockwood, G. W., & Skiff, B. A. 2007, AJ, 122, 862

Harman, C. E., Schwieterman, E. W., Schottelkotte, J. C., & Kasting, J. F. 2015, ApJ, 812, 137

Hauschildt, P. H., Allard, F., & Baron, E. 1999, ApJ, 512, 377

Hawley, S. L., Gizis, J. E., & Reid, I. N. 1996, AJ, 112, 2799

Hawley, S. L., & Johns-Krull, C. M. 2003, ApJL, 588, L109

Hawley, S. L., & Pettersen, B. R. 1991, ApJ, 378, 725

Henry, T. J., Walkowicz, L. M., Barto, T. C., & Golimowski, D. A. 2002, AJ, 123, 2002

Hilton, E. J., West, A. A., Hawley, S. L., & Kowalski, A. F. 2010, AJ, 140, 1402

Høg, E., Fabricius, C., Makarov, V. V., et al. 2000, A&A, 355, L27

Hörst, S. M., He, C., Ugelow, M. S., et al. 2018, ApJ, 858, 119

Houdebine, E. R. 2010, MNRAS, 407, 1657

Houdebine, É. R., Mullan, D. J., Doyle, J. G., et al. 2019, AJ, 158, 56

Houdebine, E. R., Mullan, D. J., Paletou, F., & Gebran, M. 2016, ApJ, 822, 97

Hu, R., Seager, S., & Bains, W. 2012, ApJ, 761, 166

Hunter, J. D. 2007, CSE, 9, 99

Husser, T. O., Wende-von Berg, S., Dreizler, S., et al. 2013, A&A, 553, A6

Irwin, J., Berta, Z. K., Burke, C. J., et al. 2011, ApJ, 727, 56

Jao, W.-C., Henry, T. J., Subasavage, J. P., et al. 2014, AJ, 147, 21

Johnson, H. L. 1966, ARA&A, 4, 193

Joy, A. H., & Abt, H. A. 1974, ApJS, 28, 1

Kiraga, M. 2012, AcA, 62, 67

Kirkpatrick, J. D., Henry, T. J., & McCarthy, D. W. J. 1991, ApJS, 77, 417

Koen, C., Kilkenny, D., van Wyk, F., & Marang, F. 2010, MNRAS, 403, 1949

Kotoneva, E., Innanen, K., Dawson, P. C., Wood, P. R., & De Robertis, M. M. 2005, A&A, 438, 957

Kraus, A. L., Shkolnik, E. L., Allers, K. N., & Liu, M. C. 2014, AJ, 147, 146

Kraus, A. L., Tucker, R. A., Thompson, M. I., Craine, E. R., & Hillenbrand, L. A. 2011, ApJ, 728, 48

Kruczek, N., France, K., Evonosky, W., et al. 2017, ApJ, 845, 3

Kukarkin, B. V., Kholopov, P. N., Artiukhina, N. M., et al. 1981, Catalogue of Suspected Variable Stars (Moscow: Acad. Sci. USSR S)

Lammer, H., Lichtenegger, H. I., Kulikov, Y. N., et al. 2007, AsBio, 7, 185

Landi, E., Young, P. R., Dere, K. P., Del Zanna, G., & Mason, H. E. 2013, ApJ, 763, 86

Landolt, A. U. 2009, AJ, 137, 4186

Laughlin, G., Bodenheimer, P., & Adams1, F. C. 1997, ApJ, 482, 420

Leenaarts, J., Carlsson, M., & Rouppe van der Voort, L. 2012, ApJ, 749, 136

Lépine, S., & Gaidos, E. 2011, AJ, 142, 138

Libby-Roberts, J. E., Berta-Thompson, Z. K., Désert, J.-M., et al. 2020, AJ, 159, 57

Linsky, J. L., Bushinsky, R., Ayres, T., Fontenla, J., & France, K. 2012, ApJ, 745, 25

Linsky, J. L., Fontenla, J., & France, K. 2013, ApJ, 780, 61

Linsky, J. L., Wood, B. E., Youngblood, A., et al. 2020, ApJ, 902, 3

Lovis, C., Dumusque, X., Santos, N. C., et al. 2011, arXiv:1107.5325

Loyd, R. O. P., & France, K. 2014, ApJS, 211, 9

Loyd, R. O. P., France, K., Youngblood, A., et al. 2016, ApJ, 824, 102

Loyd, R. O. P., France, K., Youngblood, A., et al. 2018b, ApJ, 867, 71

Loyd, R. O. P., Shkolnik, E. L., Schneider, A. C., et al. 2018a, ApJ, 867, 70

Luger, R., & Barnes, R. 2015, AsBio, 15, 119

Maldonado, J., Scandariato, G., Stelzer, B., et al. 2017, A&A, 598, A27

Malo, L., Artigau, É, Doyon, R., et al. 2014a, ApJ, 788, 81

Malo, L., Doyon, R., Feiden, G. A., et al. 2014b, ApJ, 792, 37

Malo, L., Doyon, R., Lafrenière, D., et al. 2013, ApJ, 762, 88

Mann, A. W., Feiden, G. A., Gaidos, E., Boyajian, T., & von Braun, K. 2015, ApJ, 804, 64

Martin, E. L., Rebolo, R., Magazzu, A., & Pavlenko, Y. V. 1994, A&A, 282, 503

Mauas, P. J. D., & Falchi, A. 1994, A&A, 281, 129

Mauas, P. J. D., & Falchi, A. 1996, A&A, 310, 245

Mayor, M., Pepe, F., Queloz, D., et al. 2003, Msngr, 114, 20

McCarthy, K., & White, R. J. 2012, AJ, 143, 134

McClintock, W. E., Snow, M., & Woods, T. N. 2005, SoPh, 230, 259

McKinney, W. 2010, in Proc. the IX Python in Science Conf., ed. S. van der Walt & J. Millman (Austin, TX: SciPy), 56

Meadows, V. S., Reinhard, C. T., Arney, G. N., et al. 2018, AsBio, 18, 17

Mermilliod, J. C. 1986, Catalogue of Eggen's UBV Data (Strasbourg: CDS)

Middlekoop, F. 1982, A&A, 107, 31

Miguel, Y., Kaltenegger, L., Linsky, J. L., & Rugheimer, S. 2015, MNRAS, 446, 345

Miles, B. E., & Shkolnik, E. L. 2017, AJ, 154, 67

Mittag, M., Schmitt, J. H. M. M., & Schröder, K.-P. 2013, A&A, 549, 117

Morley, C. V., Fortney, J. J., Kempton, E. M. R., et al. 2013, ApJ, 775, 33

Morley, C. V., Fortney, J. J., Marley, M. S., et al. 2015, ApJ, 815, 110

Moultaka, J., Ilovaisky, S. A., Prugniel, P., & Soubiran, C. 2004, PASP, 116, 693

Neves, V., Bonfils, X., Santos, N. C., et al. 2014, A&A, 568, A121

Newton, E. R., Charbonneau, D., Irwin, J., & Mann, A. W. 2015, ApJ, 800, 85

Newton, E. R., Irwin, J., Charbonneau, D., et al. 2016, ApJ, 821, 93

Newton, E. R., Irwin, J., Charbonneau, D., et al. 2017, ApJ, 834, 85

Noyes, R. 1984, ApJ, 279, 763

Oja, T. 1985, A&AS, 61, 331

Osten, R. A., Godet, O., Drake, S., et al. 2010, ApJ, 721, 785

Peacock, S., Barman, T., Shkolnik, E. L., Hauschildt, P. H., & Baron, E. 2019, ApJ, 871, 235

Pecaut, M. J., & Mamajek, E. E. 2013, ApJS, 208, 9

Pérez, F., & Granger, B. E. 2007, CSE, 9, 21

Plavchan, P., Werner, M. W., Chen, C. H., et al. 2009, ApJ, 698, 1068

Redfield, S., & Linsky, J. L. 2002, ApJS, 139, 439

Redfield, S., & Linsky, J. L. 2004, ApJ, 602, 776

Reid, I. N., Cruz, K. L., Allen, P., et al. 2004, AJ, 128, 463

Reid, I. N., & Gizis, J. E. 1997, AJ, 113, 2246

Reid, I. N., & Gizis, J. E. 2005, PASP, 117, 676

Reid, I. N., Hawley, S. L., & Gizis, J. E. 1995, AJ, 110, 1838

Riaz, B., Gizis, J. E., & Harvin, J. 2006, AJ, 132, 866

Ribas, I., Gregg, M. D., Boyajian, T. S., & Bolmont, E. 2017, A&A, 603, A58

Ribas, I., Tuomi, M., Reiners, A., et al. 2018, Natur, 563, 365

Riedel, A. R., Alam, M. K., Rice, E. L., Cruz, K. L., & Henry, T. J. 2017, ApJ, 840, 87

Rivera, E. J., Lissauer, J. J., Butler, R. P., et al. 2005, ApJ, 634, 625

Robertson, P., Endl, M., Cochran, W. D., & Dodson-Robinson, S. E. 2013, ApJ, 764, 3

Rojas-Ayala, B., Covey, K. R., Muirhead, P. S., & Lloyd, J. P. 2012, ApJ, 748, 93

Röser, S., Schilbach, E., Piskunov, A. E., Kharchenko, N. V., & Scholz, R. D. 2011, A&A, 531, A92

Rugheimer, S., Kaltenegger, L., Segura, A., Linsky, J., & Mohanty, S. 2015, ApJ, 809, 57

Rutten, R. 1984, A&A, 130, 353

Santos, J. F. C., Dottori, H., & Grosbøl, P. 2013, A&A, 553, A74

Sanz-Forcada, J., García-Álvarez, D., Velasco, A., et al. 2010, in IAU Symp. 264, Solar and Stellar Variability: Impact on Earth and Planets, ed. A. G. Kosovichev, A. H. Andrei, & J.-P. Rozelot (Cambridge: Cambridge Univ. Press), 478

Sanz-Forcada, J., Micela, G., Ribas, I., et al. 2011, A&A, 532, 6

Schneider, A. C., & Shkolnik, E. L. 2018, AJ, 155, 122

Scholz, R. D., Meusinger, H., & Jahreiß, H. 2005, A&A, 442, 211

Ségransan, D., Kervella, P., Forveille, T., & Queloz, D. 2003, A&A, 397, L5

Segura, A., Kasting, J. F., Meadows, V., et al. 2005, AsBio, 5, 706

Shields, A. L., Ballard, S., & Johnson, J. A. 2016, PhR, 663, 1

Shkolnik, E., Liu, M. C., & Reid, I. N. 2009, ApJ, 699, 649

Shkolnik, E. L., Allers, K. N., Kraus, A. L., Liu, M. C., & Flagg, L. 2017, AJ, 154, 69

Shkolnik, E. L., Anglada-Escudé, G., Liu, M. C., et al. 2012, ApJ, 758, 56

Shkolnik, E. L., & Barman, T. S. 2014, AJ, 148, 64

Sing, D. K., Lavvas, P., Ballester, G. E., et al. 2019, AJ, 158, 91

Stauffer, J., Tanner, A. M., Bryden, G., et al. 2010, PASP, 122, 885

Stauffer, J. R., & Hartmann, L. W. 1986, ApJS, 61, 531

Stelzer, B., Marino, A., Micela, G., Lopez-Santiago, J., & Liefke, C. 2013, MNRAS, 431, 2063

Suárez Mascareño, A., Rebolo, R., González Hernández, J. I., & Esposito, M. 2015, MNRAS, 452, 2745

Tarter, J. C., Backus, P. R., Mancinelli, R. L., et al. 2007, AsBio, 7, 30

Terrien, R. C., Mahadevan, S., Deshpande, R., & Bender, C. F. 2015, ApJS, 220, 16

Tian, F., France, K., Linsky, J. L., Mauas, P. J. D., & Vieytes, M. C. 2013, E&PSL, 385, 22

Toledo-Padrón, B., González Hernández, J. I., Rodríguez-López, C., et al. 2019, MNRAS, 488, 5145

Torres, C. A. O., Quast, G. R., da Silva, L., et al. 2006, A&A, 460, 695

Torres, G., Winn, J. N., & Holman, M. J. 2008, ApJ, 677, 1324

Tuomi, M., & Anglada-Escudé, G. 2013, A&A, 556, A111

Upgren, A. R., Grossenbacher, R., Penhallow, W. S., MacConnell, D. J., & Frye, R. L. 1972, AJ, 77, 486

19

van Belle, G. T., & von Braun, K. 2009, ApJ, 694, 1085
van der Walt, S., Colbert, S. C., & Varoquaux, G. 2011, CSE, 13, 22
Van Grootel, V., Fernandes, C. S., Gillon, M., et al. 2018, ApJ, 853, 30
van Leeuwen, F. 2007, A&A, 474, 653
Vaughan, A. H., Baliunas, S. L., Middelkoop, F., et al. 1981, ApJ, 250, 276
Vaughan, A. H., Preston, G. W., & Wilson, O. C. 1978, PASP, 90, 267
Vernazza, J. E., Avrett, E. H., & Loeser, R. 1981, ApJS, 45, 635
Virtanen, P., Gommers, R., Oliphant, T. E., et al. 2020, NatMe, 17, 261
Vogt, S. S., Allen, S. L., Bigelow, B. C., et al. 1994, Proc. SPIE, 2198, 362
von Braun, K., Boyajian, T. S., Kane, S. R., et al. 2011, ApJL, 729, L26
von Braun, K., Boyajian, T. S., Kane, S. R., et al. 2012, ApJ, 753, 171
von Braun, K., Boyajian, T. S., van Belle, G. T., et al. 2014, MNRAS, 438, 2413
Waalkes, W. C., Berta-Thompson, Z., Bourrier, V., et al. 2019, AJ, 158, 50
Walker, M. F. 1983, ApJ, 271, 642
Walkowicz, L. M., & Hawley, S. L. 2008, AJ, 137, 3297
Walkowicz, L. M., & Hawley, S. L. 2009, AJ, 137, 3297
Wargelin, B. J., Kashyap, V. L., Drake, J. J., García-Alvarez, D., & Ratzlaff, P. W. 2008, ApJ, 676, 610

Wargelin, B. J., Saar, S. H., Pojmański, G., Drake, J. J., & Kashyap, V. L. 2017, MNRAS, 464, 3281
Weinberger, A. J., Anglada-Escudé, G., & Boss, A. P. 2012, ApJ, 762, 118
Weinberger, A. J., Anglada-Escudé, G., & Boss, A. P. 2013, ApJ, 762, 118
West, A. A., Morgan, D. P., Bochanski, J. J., et al. 2011, AJ, 141, 97
White, R. J., Schaefer, G., Ten Brummelaar, T., et al. 2015, AAS Meeting, 225, 348.12
Wilson, O. C. 1963, ApJ, 138, 832
Wilson, O. C. 1968, ApJ, 153, 221
Wilson, O. C., & Vainu Bappu, M. K. 1957, ApJ, 125, 661
Wood, B. E., Redfield, S., Linsky, J. L., Mueller, H.-R., & Zank, G. P. 2005, ApJS, 159, 118
Woolf, V. M., & Wallerstein, G. 2006, PASP, 118, 218
Wordsworth, R., & Pierrehumbert, R. 2014, ApJL, 785, L20
Wylie-De Boer, E., Freeman, K., & Williams, M. 2010, AJ, 139, 636
Youngblood, A., France, K., Loyd, R. O. P., et al. 2016, ApJ, 824, 101
Youngblood, A., France, K., Loyd, R. O. P., et al. 2017, ApJ, 843, 31
Zacharias, N., Finch, C. T., Girard, T. M., et al. 2013, AJ, 145, 44
Zurlo, A., Mesa, D., Desidera, S., et al. 2018, MNRAS, 480, 35